

1 **The MAVEN EUVM Model of Solar Spectral**
2 **Irradiance Variability at Mars: Algorithms and**
3 **Results.**

Edward M. B. Thiemann,¹ Phillip C. Chamberlin,² Francis G. Eparvier,¹
Brian Templeman,¹ Thomas N. Woods,¹ Stephen W. Bougher,³ Bruce M.
Jakosky¹

Corresponding author: Edward M. B. Thiemann, Laboratory for Atmospheric and
Space Physics, University of Colorado, 3665 Discovery Drive, Boulder, CO, USA. (thie-
mann@lasp.colorado.edu)

¹Laboratory for Atmospheric and Space
Physics, University of Colorado, Boulder,
CO, USA.

²Solar Physics Laboratory, NASA
Goddard Spaceflight Center, Greenbelt,
MD, USA.

³Department of Climate and Space
Sciences and Engineering, University of
Michigan, Ann Arbor, MI, USA.

**This is the author manuscript accepted for publication and has undergone full peer review but
has not been through the copyediting, typesetting, pagination and proofreading process, which
may lead to differences between this version and the Version of Record. Please cite this article**

DOI: [10.1002/2016JA023512](https://doi.org/10.1002/2016JA023512) March 8, 2017, 11:01pm

D R A F T

Key Points.

1. A new algorithm specifies variations of solar EUV irradiance at Mars with typical relative uncertainties near 5%.
2. Daily average and flare irradiances are derived from SDO EVE measurements from 6-106 nm.
3. Examples of EUV variability for the MAVEN primary mission are presented.

4 **Abstract.** Solar Extreme Ultraviolet (EUV) radiation is a primary en-
5 ergy input to the Mars atmosphere, causing ionization and driving photo-
6 chemical processes above approximately 100 km. Because solar EUV radi-
7 ation varies with wavelength and time, measurements must be spectrally re-
8 solved to accurately quantify its impact on the Mars atmosphere. The Mars
9 Atmosphere and Volatile EvolutioN (MAVEN) EUV Monitor (EUVM) mea-
10 sures solar EUV irradiance incident on the Mars atmosphere in three bands.
11 These three bands drive a spectral irradiance variability model called the Flare
12 Irradiance Spectral Model (FISM) -Mars (-M) which is an iteration of the
13 FISM model by Chamberlin et al [2007; 2008] for spectral irradiance at Earth.
14 In this paper, we report the algorithms used to derive FISM-M and its as-
15 sociated uncertainties, focusing on differences from the original FISM. FISM-
16 M spectrally resolves the solar EUV irradiance at Mars from 0.5-189.5 nm
17 at 1 minute cadence, and 0.1 nm resolution in the 6-106 nm range or 1 nm
18 resolution otherwise. FISM-M is suitable for both daily average and flaring
19 spectral irradiance estimates; and is based on the linear association of the
20 broadband EUVM measurements with spectral irradiance measurements, in-

21 cluding recent high time cadence 0.1 nm resolution measurements from the
22 EUV Variability Experiment (EVE) on the Space Dynamics Observatory (SDO)
23 between 6 and 106 nm. In addition, we present examples of model outputs
24 for EUV irradiance variability due to solar flares, solar rotations, Mars or-
25 bit eccentricity and the solar cycle, between October, 2015 and November
26 2016.

Author Manuscript

1. Introduction

27 Mars is believed to have once had substantial amounts of flowing water which would
28 have required a thicker and warmer atmosphere than is currently present (e.g. Jakosky
29 & Phillips [2001]; Carr & Head [2003]). All planets lose some portion of their atmosphere
30 to space and those that lack a global magnetic field, like Mars, are particularly sensitive
31 to erosion by the solar wind, which would otherwise be deflected around a planet with
32 a strong global magnetic field (Chassefière & Leblanc [2004]). As such, Mars could have
33 lost a significant fraction of its atmosphere and water to space over time. The National
34 Aeronautics and Space Administration (NASA) sent the Mars Atmosphere and Volatile
35 Evolution (MAVEN) spacecraft to Mars to characterize the mechanisms and magnitude
36 of atmospheric escape in the current epoch in order to better understand how the Martian
37 atmosphere has evolved over time (Jakosky et al. [2015]).

38 MAVEN was launched on 18 November 2013 and began its primary science mission at
39 Mars on 17 November 2014. MAVEN is instrumented to characterize the Mars upper
40 atmosphere and plasma environment as well as the solar drivers that influence it, pro-
41 viding a single platform to measure both escaping atoms and ions and the drivers that
42 lead to escape. The MAVEN orbit is highly elliptical with apoapsis near 6000 km and
43 periapsis near 150 km, and it precesses so that in-situ periapsis measurements sample
44 the thermosphere and ionosphere over a range of local times and latitudes, or conversely
45 in situ apoapsis measurements sample a range of regions of the near space environment,
46 including the solar wind, magnetosheath and magnetotail.

47 Along with the solar wind, solar extreme ultraviolet (EUV, 6-120 nm) radiation is a pri-
48 mary energy input to the Mars upper atmosphere; heating the thermosphere, creating the
49 ionosphere and constraining processes that lead to atmospheric escape to space (Bougher
50 et al. [2015a]). Photons with wavelengths below approximately 100 nm are strongly ab-
51 sorbed by neutral CO₂ and O, which together constitute the major species of the Mars
52 upper atmosphere. The abundance of these species results in total absorption of the solar
53 EUV spectrum above approximately 100 km with peak energy deposition occurring near
54 150 km (Haider & Mahajan [2014]).

55 MAVEN characterizes the solar EUV radiation input at Mars with the Extreme Ultra-
56 violet Monitor (EUVM), a sensor on the Langmuir Probes and Waves (LPW) instrument
57 (Eparvier et al. [2015]). EUVM has three calibrated photometers that measure solar
58 irradiance at Mars in the 0-7 nm, 17-22 nm and 117-125 (full width at half maximum
59 (FWHM)) bands at 1 second cadence. Solar irradiance is defined as the solar radiated
60 power per unit area incident on a surface or, in the case of spectral irradiance, power per
61 unit area per unit wavelength with SI units of Wm^{-2} or $Wm^{-2}nm^{-1}$, respectively. The
62 EUVM bands were selected to measure variability in three different regions of the solar
63 atmosphere, and serve as proxies, or inputs, for an EUV spectral model from 0.5-189.5
64 nm with 0.1 nm resolution from 6-106 nm and 1 nm resolution otherwise. Here, we adopt
65 a convention similar to that of Tobiska et al. [2000] and Chamberlin *et al.* [2007; 2008],
66 and define a proxy to be any solar measurement that is used in combination with regres-
67 sion coefficients to estimate solar spectral irradiance variability. They can be of non-EUV
68 origin such as sunspot number or 10.7 cm solar radio flux (F10.7), or they can be EUV
69 measurements such as the three MAVEN EUVM bands. The 3 calibrated irradiances that

70 are used as inputs to the EUVM spectral model are reported in the EUVM Level 2 data
71 product, and the modeled spectral irradiance variability at Mars is produced by the Flare
72 Irradiance Spectral Model (FISM)-Mars (M) and reported as part of the Level 3 data
73 product. FISM-M is the focus of this paper, and consists of daily and flare irradiance
74 variability model components which will be presented separately.

75 FISM-M is the MAVEN EUVM spectral model, and is an iteration of FISM developed
76 by Chamberlin *et al.* [2007; 2008]. We will refer to the original FISM by Chamberlin
77 *et al.* [2007; 2008] as FISMv1 to avoid confusion. Both FISMv1 and FISM-M model
78 irradiance empirically with a set of linear regression coefficients that relate available prox-
79 ies to spectral irradiance measurements, and are found by the method of least squares.
80 This is the same basic method used by earlier empirical EUV spectral irradiance variabil-
81 ity models, which include Hinteregger81 (Hinteregger *et al.* [1981]), EUVAC (Richards
82 *et al.* [1994]), EUV97 (Tobiska & Eparvier [1998]), Solar2000 (Tobiska *et al.* [2000]) and
83 HEUVAC (Richards *et al.* [2006]).

84 FISM-M advances daily and flare empirical irradiance variability modeling by relating
85 measurements of EUV irradiance variations in broad spectral bands to spectral irradiance
86 measurements in the 6-106 nm range made by the EUV Variability Experiment (EVE)
87 (Woods *et al.* [2012]), which is onboard the Solar Dynamics Observatory (SDO) satellite
88 launched on 11 February 2010, and has improved spectral and temporal resolution as well
89 as an improved responsivity calibration accuracy compared to its predecessor, TIMED
90 SEE (Woods *et al.* [2000], Hock *et al.* [2012]). The 6-106 nm range is measured by EVE
91 with the Multiple EUV Grating Spectrographs (MEGS) at 0.1 nm resolution and 10 second
92 time-cadence. MEGS observed the Sun nearly continuously in the 6-37 nm range until 27

93 May 2014, after which the channel suffered a failure resulting in the loss of observations
94 in this spectral range. MEGS continues to make solar observations in the 35-106 nm
95 range for 5 continuous minutes every hour which are supplemented with varying daily
96 campaigns of extended continuous coverage lasting 3 to 24 hours. In addition to including
97 the 6-27 nm range not spectrally resolved by SEE EGS, EVE MEGS measurements in
98 the 6-106 nm range are an improvement over those of SEE EGS by having 10X better
99 spectral resolution (0.1 nm vs 1 nm) and continuous observations at 10 second cadence
100 compared with the 3 minute observation periods every 100 minutes at 10 second cadence
101 made by TIME SEE. SDO EVE's improved observation cadence is suitable for measuring
102 flare irradiance, which can vary by tens to hundreds of percent over a period of minutes
103 and last tens of minutes to hours (depending on wavelength and flare magnitude). With
104 regard to improved uncertainty, the MEGS responsivity is known to within 1-3% ($1-\sigma$)
105 uncertainty below 80 nm from pre-flight calibrations (Hock et al. [2012]); in comparison
106 with the 3-7% ($1-\sigma$) preflight responsivity uncertainty of SEE EGS (Woods et al. [2005]).

107 FISM-M has been widely used in the analysis of MAVEN results. For example, Rahmati
108 et al. [2015] used EUV spectra to estimate ionization rates used in a model of O pickup
109 ions; Chaffin et al. [2015], Chaufray et al. [2015], Jain et al. [2015], Evans et al. [2015],
110 and Deighan et al. [2015] used EUV and Far Ultraviolet (FUV, 120-190 nm) spectra to
111 interpret airglow brightnesses measured by the MAVEN Imaging Ultraviolet Spectrograph
112 (IUVS); and Sakai et al. [2016] and Peterson et al. [2016] used EUV spectra to estimate
113 photoelectron production.

114 Given its improvements over FISMv1 and applicability to the analysis of MAVEN re-
115 sults, it is important to demonstrate the capabilities and limitations of the FISM-M

116 data product. This paper describes the calibration and algorithms used to produce the
117 MAVEN EUVM FISM-M data product, Version 8 Revision 1, and reports its uncertainties
118 and caveats. Although the model and results reported here are specific to irradiance at
119 Mars as observed by MAVEN EUVM, they include the first reported spectral irradiance
120 variability model based on the EVE dataset and should be of interest to the broader solar
121 irradiance and terrestrial upper atmosphere research communities.

122 This paper is outlined as follows, we motivate the need for spectral irradiance modeling
123 at Mars by describing EUV variability at Mars, followed by a review of the data and
124 sources used to develop and run FISM-M. We then provide a detailed description of FISM-
125 M, reporting the model uncertainty and caveats. Next, FISM-M irradiance variability
126 results from the MAVEN mission are reported, which include a model of where in the
127 Mars atmosphere EUV energy is absorbed as a function of altitude and wavelength. We
128 finish the paper by discussing future improvements to the FISM-M data product.

2. Estimates and Measurements of EUV Irradiance Variability at Mars

129 The solar EUV spectrum consists of series of emission lines and ionization continua
130 emitted from ionized gases in the solar chromosphere, transition region and corona. Below
131 10 nm, thermal bremsstrahlung continua can become significant (Phillips et al. [2008]).
132 The EUV spectrum is loosely defined as ranging from 6-120 nm, bracketed by the Soft X-
133 Ray (SXR) and Far Ultraviolet (FUV) regions on the short and long edges, respectively;
134 both of which also deposit energy into the upper atmosphere of Mars (Bougher et al.
135 [2015a]). EUV radiation varies significantly on timescales of minutes from solar flares,
136 days from solar rotation, and years from the solar cycle (Lean [1997]). The effect of
137 solar activity on the EUV spectrum is not uniform, with shorter wavelengths tending

138 to be more variable than longer wavelengths (Woods et al. [2005], Woods et al. [2015]).
139 This spectral dependence on variability is a result of the shorter wavelengths primarily
140 originating in the more variable corona compared to the longer wavelengths which are
141 primarily of chromospheric origin. Because the constituent gas ionization cross-sections
142 also vary as a function of wavelength, EUV radiation must be spectrally resolved to
143 accurately characterize the effect it has on the Mars upper atmosphere. Mars's orbit
144 eccentricity adds an additional 687 day (1 Mars year) variability cycle as the Mars-Sun
145 distance changes from 1.38 to 1.67 AU. This should be contrasted with the Earth-Sun
146 distance which varies from 0.983-1.017 AU over an Earth year. Both seasonal and solar
147 cycle EUV variability is expected to be a major source of variability in the Mars upper
148 atmosphere (Bougher et al. [2015a] , Bougher et al. [2016]).

149 EUV irradiance at Earth and Mars differs for two primary reasons. First, irradiance
150 falls off inversely with the square of the distance from the Sun. As such, irradiance at
151 Mars is 36-53% of that at 1 AU compared with irradiance at Earth which varies from 96.7-
152 103.4% of the 1 AU value due to the planetary orbit eccentricity. Because EUVM data
153 products are primarily intended to be used for characterizing the Mars atmosphere and
154 the Mars orbit eccentricity is a significant contributor to irradiance variability at Mars, we
155 report irradiance scaled to the center-to-center Mars-Sun distance unless otherwise stated
156 in this paper. The second reason EUV irradiance at Earth and Mars differ is because
157 EUV radiation originates from inhomogeneous features in the Sun's atmosphere such as
158 active regions, and the solar hemisphere visible from Mars may have more or less EUV
159 source regions than the solar hemisphere visible from Earth. These solar features appear
160 to migrate across the observed solar disk due to solar rotation, which varies with latitude

161 and has a sidereal period of 24.4 days at the equator and 38 days at the poles. Carrington
 162 [1858] discovered activity regions tended to be confined to certain latitudes that rotate
 163 with a sidereal period equal to 25.38 days, now known as the Carrington Period, and
 164 causes irradiance variability at this time scale.

2.1. Estimating Irradiance at Mars from Earth Measurements

165 Irradiance can be estimated at Mars by linearly interpolating measurements from Earth
 166 made before and after the face of the Sun rotates past Mars for a particular day of interest
 167 if we assume the source regions rotate with a constant 25.38 day period. A description of
 168 the interpolation scheme follows, using the geometrical definitions indicated in Figures 1a
 169 and 1b, where Ω_s is the solar rotation frequency taken to be $2\pi/25.38$ radian/day and Ω_E
 170 is the Earth orbital rate taken to be $2\pi/365.25$ radian/day. The interpolated irradiance
 171 at 1AU for the hemisphere of the Sun facing Mars with a Mars-Sun-Earth angle $\Theta_{ME}(t_d)$
 172 for day t_d is given by

$$E_M(t_d, \Theta_{ME}) = (w_1 E_E(t_d - \Delta t_1) + w_2 E_E(t_d + \Delta t_2)) R_M(t_d)^{-2} \quad (1)$$

173 where E_E is measured at Earth and scaled to 1 AU. Θ_{ME} is defined with counter-clockwise
 174 rotation being positive, and $R_M(t_d)$ is the Mars-Sun distance in units of AU (on day t_d);
 175 values of Θ_{ME} and R_M for the first 2.25 years of the Mars mission are shown in Figures
 176 1c and 1d.

177 Beginning with the definitions in Figure 1a, we can express ϕ_1 in terms of the time
 178 difference Δt_1 .

$$\phi_1 = \Omega_E \cdot \Delta t_1 \quad (2)$$

179 The face of the Sun rotates an angle ϕ_2 from Earth on day $t_d - \Delta t_1$ to Mars on day t_d at
 180 angular speed Ω_S , allowing us to write,

$$\phi_2 = \Omega_S \cdot \Delta t_1. \quad (3)$$

181 From Figure 1a, we see that $\phi_2 = \phi_1 + \Theta_{ME}$. Substituting Equations (2) and (3) into this
 182 expression and solving for Δt_1 yields

$$\Delta t_1 = \frac{\Theta_{ME}(t_d)}{\Omega_s - \Omega_E}. \quad (4)$$

183 Similar arguments can be made starting with the geometry in Figure 1b to derive the
 184 following expression for Δt_2 ,

$$\Delta t_2 = \frac{2\pi - \Theta_{ME}(t_d)}{\Omega_s - \Omega_E}. \quad (5)$$

185 The weights are given by

$$w_{1,2} = \frac{\Delta t_{2,1}}{27.27}. \quad (6)$$

186 Note that interpolated measurements with larger time differences have smaller weights.

187 Prior to the arrival of MAVEN EUVM at Mars, the above described interpolation
 188 method was needed to estimate solar irradiance incident on the Mars atmosphere from
 189 observations made at Earth. Solar active region emission intensity evolves non-linearly

190 (Aschwanden [2006]) and linear interpolation of their emitted irradiance is prone to error.
191 Further, the effects of variability over very short time-scales such as those of flares can
192 only be studied if the emitting region (e.g. flaring site) is visible from both planets.
193 The newly available EUV irradiance measurements at Mars made by EUVM provide
194 new opportunities to study the effects of short-term EUV irradiance variability and are
195 independent of the error associated with linear interpolation.

2.2. Direct Broadband Irradiance Measurements at Mars from MAVEN EUVM

196 Since long term spectral irradiance measurements used to cross-calibrate any empiri-
197 cal model of solar spectral irradiance variability are only available at Earth, the MAVEN
198 EUVM channels must be cross-calibrated against comparable channels in orbit at Earth in
199 order to be used as inputs to FISM-M. Figures 2a, 2c and 2e compare time series of daily
200 irradiance measurement averages made by the three EUVM channels with the those mea-
201 sured by the Earth-based channels against which they are cross-calibrated. The EUVM
202 data are shown with thick red lines whereas the Earth measurements are shown with thin
203 blue lines and have been scaled to $R_M(t)$. The measurement bands are shown above each
204 panel. The 0-7 nm and 17-22 nm EUVM bands are cross-calibrated against the 0-7 nm
205 and 17-22 nm bands measured by the EUV SpectroPhotometer (ESP) (Didkovsky et al.
206 [2012]), which is part of the SDO EVE instrument suite. The cross-calibration is achieved
207 by a simple first order linear least squares fit of the EUVM in-band counts with the ESP
208 measurements that have been interpolated to Mars using Equation (1). Neither of these
209 two bands show signs of optical degradation based on the linear relationship with their
210 Earth measured (and degradation corrected) counterparts. The 117-125 EUVM band is

211 cross-calibrated with 121.6 nm H I Lyman-alpha measurements made by the SOLar STel-
212 lar Irradiance Comparison Experiment (SOLSTICE) onboard the Solar Radiation and
213 Climate Experiment (SORCE) (McClintock et al. [2000]). This EUVM band shows some
214 degradation with an exponential decay time constant of 2,252 days. The cross-calibration
215 of the 117-125 band is done by first interpolating SOLSTICE measurements to Mars using
216 Equation (1). Next, average ratios of the SOLSTICE irradiance to EUVM counts for the
217 first 60 days EUVM measurements are available are used to find the initial instrument
218 response. The degradation function decay constant is found using average ratios of the
219 irradiance to counts over the 60 days near Earth-Mars opposition (22 May 2016) to de-
220 termine the decay constant. Note that approximately 90% of the signal measured by the
221 117-125 nm EUVM band lies in the 121-122 nm range and the cross-calibration with SOL-
222 STICE Lyman-alpha measurements implies that reported irradiances are for the 121.6 nm
223 Lyman-alpha emission line. As such, this band is also referred to as the Lyman-alpha or
224 121.6 nm band.

225 The time series in Figures 2a, 2c and 2e capture the three dominant components of
226 spectral EUV variability at Mars. The short term oscillations are due to solar rotation
227 and have a calculated synodic Carrington Period at Mars of approximately 26.35 days,
228 which is shorter than the calculated 27.28 day period for Earth because of Mars's longer
229 orbital period. The steep decrease in irradiance from late 2014 through late 2015 is due to
230 a combination of the declining solar cycle and increasing $R_M(t)$. Mars reached aphelion
231 on 20 November 2015. As such, the irradiance decreased to a lesser degree as $R_M(t)$ began
232 to decrease. Beginning in 2016, an irradiance increase can be seen in the 17-22 nm and
233 121.6 nm bands indicating the variability due to $R_M(t)$ is dominating (matching) the solar

234 cycle decline for the 121.6 nm (17-22 nm) band during this period. On the other hand,
235 the 0-7 nm band continues to decrease indicating the solar cycle decline is slightly larger
236 than the $R_M(t)$ variability for this band.

237 Figures 2b, 2d and 2f show scatter plots of the EUVM measurements and the Earth-
238 based measurements against which the EUVM bands are calibrated. Note that all data
239 are scaled to 1 AU. To remove error induced from solar rotations, Earth measurements
240 are angularly interpolated to Mars using Equation (1). Because Equation (1) does not
241 account for variability occurring at hourly and daily time-scales due to solar active re-
242 gion emergence and flares, both EUVM and Earth data are smoothed with an 81 day
243 (approximately 3 solar rotations) moving average to find the long-term cross-calibration
244 uncertainty. The 1:1 line is shown with a dotted line and the standard deviation from
245 this line are reported on each panel in percent, and are 2.6% for both the 0-7 nm and
246 17-22 nm bands, and 2.1% for the 121.6 nm band. We take these standard deviations to
247 be the long-term cross-calibration uncertainty. Note that the measurement noise, as mea-
248 sured in-flight at 1-second cadence, is less than 0.02% and considered negligible (Thiemann
249 [2016a]).

250 This cross-calibration allows FISM-M to be implemented using the EUVM bands. The
251 methodology is described Section 4 in detail, but is briefly sketched here. Regression
252 coefficients are found between spectral irradiance measurements (e.g. SDO EVE) and the
253 three aforementioned ESP and SOLSTICE measurements. The regression coefficients are
254 then used to find the irradiance at Mars with the EUVM bands. Next, we describe the
255 data used to develop and drive FISM-M followed by a description of the FISM-M model.

3. Data Sources

3.1. MAVEN EUVM

256 FISM-M uses measurements from MAVEN EUVM, when available, to estimate spectral
257 irradiance at Mars. MAVEN EUVM measures solar irradiance in three bands selected to
258 characterize EUV emissions from distinctly different regions of the solar atmosphere. The
259 0.1-7 nm band measures irradiance from hot coronal sources, and solar flares in particular;
260 the 17-22 nm band measures irradiance from the non-flaring corona; and the band centered
261 on 121.6 nm measures the bright H I Lyman- α line which is formed in the chromosphere
262 and transition region and forms at temperatures ranging from approximately 6,000 K to
263 25,000 K (Aschwanden [2006]). The 0-7 nm and 17-22 nm EUVM bands are sensitive to
264 plasmas that form at approximately 6.3-16 MK and 0.3-2.0 MK (FWHM), respectively, as
265 determined by convolving the channel response functions with synthetic isothermal solar
266 plasma spectra from the CHIANTI atomic database (Landi et al. [2011]).

267 The EUVM measurement cadence is 1 second, and EUVM measures solar irradiance
268 continuously except when MAVEN is in eclipse, or when both MAVEN is below 500 km
269 and the Sun is in the direction of spacecraft motion. The approximate solar measurement
270 duty cycle is 60% or 2.7 (typically continuous) hours out of every 4.5 hour orbit. EUVM
271 also has reduced observations during deep dip campaigns when the spacecraft lowers
272 periapsis 15-30 km below its nominal 150 km periapsis to make in-situ measurements
273 near the homopause. These occurred approximately every 3 months for the first 2 years
274 that MAVEN was at Mars. Periods of extended data outages are evident by the gaps in
275 EUVM time series shown in Figure 2.

276 This paper uses and discusses the Version 8, Revision 1 MAVEN EUVM Level
277 2 and FISM-M data products. These datasets are publicly archived and dis-
278 tributed by the NASA Planetary Data System, Planetary Plasma Interactions Node
279 (<http://ppi.pds.nasa.gov>).

3.2. Spectral Irradiance Data

280 The spectral irradiance datasets used to find the proxy regression coefficients, or cal-
281 ibrate, FISM-M from 0.1-6 nm and above 106 nm use data from SORCE, SEE and the
282 Upper Atmosphere Research Satellite (UARS) and are discussed in Chamberlin [2007;
283 2008]. From 6-106 nm, FISM-M is calibrated against SDO EVE Version 5 data at 0.1 nm
284 resolution made by the MEGS A and B channels, and this spectral range is the focus of
285 this paper. The MEGS A channel has (absolute) uncertainties ranging from 10-20%. The
286 MEGS B channel has (absolute) uncertainties near 6% for the bright emission lines, the
287 intermediate intensity lines have uncertainties between 10-20%, and the low signal inter-
288 line regions have uncertainties from 40-100%. Above 93 nm, the interline uncertainties
289 exceed 100% because of very low signals and instrument degradation. The FISM-M Daily
290 Model uses Level 3 data from the start of the EVE mission on 3 April 2010 until the
291 failure of the 6-37 nm channel (MEGS A) on 27 May 2014; this failure also corrupted the
292 Version 5 calibration of 35-105 nm channel (MEGS B). The FISM-M Flare Model uses
293 flares with a Geostationary Operational Environmental Satellite (GOES) X-Ray Sensor
294 (XRS) classification of M-Class or greater (Bornmann et al. [1996]) appearing in the SDO
295 EVE Level 2 Version 5 data, resulting in 431 flares in the 6-37 nm range and 66 flares in
296 the 37-106 nm range. The reduced number of flares on the longer wavelength channel is
297 due to a reduced duty cycle of MEGS B discussed in Section 1.

3.3. Proxy Data

As previously stated, FISM-M is calibrated using measurements available at Earth and implemented using the EUVM channels to predict irradiance at Mars; this results in a need for two distinct types of proxies which we distinguish by the names Calibration (CAL) and Operation (OP) proxies. The Level 2 data from the EUVM Channels are the nominal OP proxies. If EUVM data are unavailable, OP proxies are interpolated from Earth using Equation (1). The proxies against which the EUVM channels are calibrated are continuing to be measured and, if available, are used as redundant OP proxies. Otherwise, the Bremen Composite Mg II core-to-wing ratio (c/w) (Snow et al. [2014]) and F10.7 radio flux (reported by the Dominion Radio Astrophysical Observatory in Penticton, British Columbia) are used.

Table 1 shows this hierarchy, and the proxies and data versions used. The second and third columns show the CAL proxies used to find regression coefficients with the EVE, SORCE and SEE spectral irradiance datasets. Table 1 also captures the following redundancy sequence: If the Primary OP Level 2 proxy are unavailable, the Secondary OP proxy in the same row is used. If the Secondary OP proxy is also not available, then the Tertiary OP proxy in the same row is used. If the Tertiary OP proxy is also unavailable, the sequence repeats with the Tertiary OP proxy in place of the Primary OP proxy in column 1. For example, if the Tertiary OP proxy is Level 2 17-22 nm and it is also unavailable, the SDO ESP v5 17-22 nm data are used if available. Ultimately, Mg II c/w is used, and if it is unavailable, F10.7. Note, flags in the publicly released EUVM spectral irradiance data indicate whether EUVM or Earth measurements are used as model inputs.

4. FISM-M Model Description

FISM-M is designed to use the MAVEN EUVM channels as proxies to drive the model directly from measurements at Mars. Aside from the input proxies, the primary difference between FISM-M and FISMv1 is in the 6-106 nm range, where different spectral irradiance datasets are used to calibrate the model. FISMv1 models spectral irradiance from 0.1-190 nm at 1 nm resolution and has been calibrated using TIMED SEE from 0.1-117 nm and UARS SOLSTICE above 117 nm. FISM-M is similar to FISMv1 outside of 6-106 nm but the FISMv1 legacy regression coefficients are scaled to match the calibration of the EUVM channels which adds additional uncertainty. In the 6-106 nm range, FISM-M has improved 0.1nm resolution and is calibrated by SDO EVE. In the current version, the 0.1 nm model output is re-binned to 1 nm for release in the EUVM FISM-M data product, but future releases and studies may include the 0.1 nm resolution version. Therefore, 0.1 nm model results and uncertainties are also presented in this section.

FISM-M decomposes the spectral irradiance at 1 AU for the i^{th} wavelength bin, $E(\lambda_i, t)$, over 4 time-scales according to Equation (7).

$$E(\lambda_i, t) = E_{min,i} + \Delta E_{sc,i} + \Delta E_{sr,i} + \Delta E_{IP,i} + \Delta E_{GP,i}, \quad (7)$$

where $E_{min,i}$, $\Delta E_{sc,i}$ and $\Delta E_{sr,i}$ are the solar minimum, solar cycle and solar rotation terms that together constitute the daily irradiance model and are described in Section 4.1. $\Delta E_{IP,i}$ and $\Delta E_{GP,i}$ are the impulsive and gradual phase flare terms that together constitute the flare irradiance contribution to the total irradiance, and are described in Section 4.2. FISM-M also decomposes the input proxies into the same components, and finds regression coefficients between the spectral irradiance and proxies for each term on

340 the right-hand side of Equation (7) at 1 AU. Since Equation (7) estimates irradiance at
 341 1 AU, it must be scaled by $1/R_M^2(t)$ to estimate the irradiance at Mars. As previously
 342 stated, all reported EUVM data products are scaled to the Mars-Sun distance.

343 It is important to note that although FISM-M results are produced at 1 minute cadence,
 344 the 1 minute data are calibrated for flare irradiance and currently do not accurately model
 345 non-flaring sub-daily variability.

346 In the remainder of this section, the FISM-M daily and flare model descriptions are
 347 presented separately because investigations tend to focus on an atmosphere's response
 348 to variability at one of these time-scales but typically not both. Each subsection (4.1
 349 for the daily model and 4.2 for the flare model) is organized identically with algorithms,
 350 model calibration, model uncertainty, and special measures for adapting FISMv1 legacy
 351 regression coefficients in sub-sub-sections 4.X.1, 4.X.2, 4.X.3 and 4.X.4, respectively.

4.1. FISM-M Daily Model Description

4.1.1. Daily Model Algorithms

352 The FISM-M daily irradiance for the i^{th} wavelength bin is given by the first three terms
 353 on the right-hand side of Equation (7) where the solar cycle and rotation terms are written
 354 explicitly as
 355

$$\Delta E_{sc,i} = \langle E_{d,i} \rangle_{108} - E_{min,i} \quad (8)$$

356 and

$$\Delta E_{sr,i} = E_{d,i} - \langle E_{d,i} \rangle_{108} \quad (9)$$

357 where $E_{d,i}$ is the daily minimum irradiance and $\langle E_{d,i} \rangle_{108}$ is its 108-day average. The
 358 terms are modeled by the following set of first-order linear equations relating them to the
 359 j^{th} solar cycle and rotation proxies, $P_{sc,j}$ and $P_{sr,j}$, respectively;

$$\Delta E_{sc,i} = E_{min,i} (b_{sc,ij} + m_{sc,ij} P_{sc,j}) \quad (10)$$

360 and

$$\Delta E_{sr,i} = E_{min,i} (b_{sr,ij} + m_{sr,ij} P_{sr,j}), \quad (11)$$

361 where, using the same notation as in Equations (8) and (9),

$$P_{sc,j} = \frac{\langle P_j \rangle_{108} - P_{min,j}}{P_{min,j}} \quad (12)$$

362 and

$$P_{sr,j} = \frac{P_{d,j} - \langle P_j \rangle_{108}}{P_{min,j}}. \quad (13)$$

363 $b_{sc,ij}$ and $m_{sc,ij}$ are the (offset and slope) regression coefficients for modeling the solar
 364 cycle component (with the i^{th} wavelength bin with the j^{th} proxy), and $b_{sc,ij}$ and $m_{sc,ij}$ are
 365 the regression coefficients for modeling the solar rotation component.

366 4.1.2. Daily Model Calibration

367 SDO EVE did not observe solar minimum. Instead, $E_{min,i}$ is found for each 0.1 nm
 368 bin by finding the spectral bin minimum daily average values for the entire calibration
 369 period and the corresponding MgII c/w values for those days. Regression coefficients

370 were found from these values that were used to estimate $E_{min,i}$ from the measured solar
 371 minimum value of MgII c/w. Since Equations (8) and (9) are over-constrained, $E_{min,i}$
 372 is not necessarily the best estimate for the minimum irradiance; rather, it is the best
 373 estimate of the minimum irradiance from the MgII c/w proxy that is modified with the
 374 regression coefficients found using other, possibly better, proxies. For the j^{th} proxy, the
 375 model predicted minimum irradiance is given by $E_{min,i} \cdot (b_{sc,ij} + b_{sr,ij})$ if we assume the
 376 solar rotation contribution approaches zero at solar minimum. It should be noted that
 377 observations suggest different wavelengths reach solar cycle minimum irradiance values at
 378 different times (Thuillier et al. [2014]), an effect that can only be reproduced if a model
 379 bin shares the same minimum time with the OP proxy.

380 The m and b terms in Equations (10) and (11) are the model coefficients found by
 381 linear least-squares fitting of the available CAL proxy and 0.1 nm resolution spectral
 382 irradiance data. 109 wavelength bins were too noisy to find meaningful fit coefficients.
 383 These excessively noisy bins were identified as bins having $m_{sc,ij} < 0$, indicating that a
 384 decreasing measured signal due to uncorrected degradation in the EVE data is masking the
 385 expected increasing true signal due to the advancing solar cycle towards solar maximum
 386 apparent in the CAL proxy data. Rather than use these known spurious coefficients, $b_{sc,ij}$
 387 is set to 0 and $m_{sc,ij}$ is set equal to $m_{sr,ij}$ for these bins because the long term degradation
 388 is expected to be subtracted from $\Delta E_{sr,i}$ with the removal of the long term solar cycle
 389 variability. We do not quantify the impact of this substitution *a priori*, but it is likely
 390 finite because $m_{sc,ij}$ and $m_{sr,ij}$ are equivalent only if P_j and E_i are formed at similar
 391 temperatures in the Sun's atmosphere (Chamberlin et al. [2007]). It is also important to
 392 note that setting $b_{sc,ij}$ to 0 can lead to increased model error near solar minimum where

393 this term is expected to become more relevant. However, because these bins correspond
 394 with the lowest irradiance in the 6-106 nm range and are multiple orders of magnitude less
 395 intense than much of the EUV spectrum, high uncertainties in these bins have minimal
 396 impact on the total EUV irradiance as is demonstrated in Section 4.1.3. The added
 397 uncertainty due to low EVE signal levels and uncorrected degradation is quantified in the
 398 EVE data product measurement accuracy, and the added model error resulting from the
 399 modified solar cycle regression coefficients is quantified in the FISM-M model uncertainty.
 400 Both of these values are incorporated into the FISM-M uncertainty and are discussed in
 401 Section 4.1.3.

402 The primary proxy for each 0.1 nm bin is found by evaluating the model at Earth for
 403 each proxy for every day that spectral irradiance data are available. The model results
 404 are then compared with measurements to select the proxy that minimizes the error for
 405 each wavelength bin. The figure of merit used is the standard deviation of the model and
 406 measurement fractional difference,

$$\sigma_{i,j} = \frac{1}{N} \sqrt{\sum_{d=0}^{N_d} \left(\frac{E_{i,j}(t_d) - E_{i,eve}(t_d)}{E_{i,eve}(t_d)} \right)^2}, \quad (14)$$

407 where $E_{i,j}$ and $E_{i,eve}$ the j^{th} proxy estimated and EVE measured irradiance for the i^{th}
 408 wavelength bin, respectively. $\sigma_{i,j}$ is also taken to be the uncertainty of the model daily
 409 irradiance prediction for the j^{th} proxy.

410 It is important to note that a smaller $\sigma_{i,j}$ does not necessarily indicate better model
 411 performance (Von Storch & Zwiers [2001]). We use the F-test to test whether differences
 412 in the model-measurement standard deviations are statistically significant and, implicitly,
 413 whether the selected primary proxy model with standard deviation, $\sigma_{i,1}$, is expected to

414 perform better than the proxy model with the second-smallest standard deviation, $\sigma_{i,2}$.

415 The F-test is implemented by computing

$$\mathbf{F} = \frac{\sigma_{i,2}^2}{\sigma_{i,1}^2}, \quad (15)$$

416 and comparing it with the critical value, \mathbf{f} , for the $F(N_2 - 1, N_1 - 1)$ distribution with
 417 10% significance level, where N_2 and N_1 are the number of samples used to compute $\sigma_{i,2}^2$
 418 and $\sigma_{i,1}^2$, respectively. If $\mathbf{F} > \mathbf{f}$, the primary proxy is no better than the proxy with the
 419 second-smallest standard deviation in only 10% of cases. Although FISM-M always uses
 420 the proxy with the smallest $\sigma_{i,j}$, the F-test is needed in order to make inferences from the
 421 data as is done in the next sub-section.

422 4.1.3. Daily Model Uncertainty

423 Figure 3 shows the model uncertainty for each 0.1 nm bin driven by each of the three
 424 CAL proxy versions of the EUVM bands. The uncertainty is given in percent, absolute
 425 units and 1nm-binned percent in Panels a, b and c; respectively. The triangles at the bot-
 426 tom of Panel a correspond with bins where the primary proxy model is not distinguishably
 427 better than the proxy model with the second-smallest standard-deviation as determined
 428 by the F-test. This occurs for 249 bins. For each 0.1 nm bin, the primary proxy is that
 429 with the lowest uncertainty shown in Figure 3a. The 1nm-binned uncertainty, $\sigma_{j,nm}$, is
 430 the signal weighted average of the initial 0.1nm-binned uncertainties, $\sigma_{i,j}$,

$$\sigma_{j,nm} = \frac{\sum_{i=j-0.55}^{i=j+0.45} \sigma_{i,j} \cdot E_{i,fism}}{\sum_{i=j-0.55}^{i=j+0.45} E_{i,fism}}. \quad (16)$$

431 Panel a shows that the statistically optimal proxies (those with statistically significant
 432 smaller standard-deviations) are consistent with the expectation that emissions originating
 433 from similar regions in the Sun's atmosphere vary similarly (Hinteregger et al. [1981]).
 434 Examining wavelengths below 60 nm, where the F-test identified significant differences
 435 in the proxy model variances, we see the 17-22 nm proxy is the optimal proxy for most
 436 bins from 6-60 nm. This is consistent with the fact that many of the bins in this region
 437 are dominated by emissions from 0.3 MK or hotter plasmas (Phillips et al. [2008]) and
 438 within the temperature range that the 17-22 nm band is sensitive. However, there are
 439 important exceptions where the 121.6 nm band is the statistically optimal proxy, such as
 440 the bright He I and II lines at 58.4 nm and 30.4 nm, respectively, and the He I continuum
 441 short-ward of 50.43 nm. In addition, the 121.6 nm band is also the statistically optimal
 442 proxy at the H continuum starting short-ward of 92 nm. These H and He emissions form
 443 at temperatures more similar to that of the 121.6 nm band and this band is, therefore,
 444 expected to be the statistically optimal proxy for these emissions.

445 The total uncertainty for the FISM-M daily irradiance, $\sigma_{i,d,total}$, is the quadrature sum
 446 of the uncertainties of the model, the EVE absolute calibration ($\sigma_{i,eve}$), and the intercali-
 447 bration of the EUVM channels and the proxies used to calibrate FISM-M ($\sigma_{j,euv}$),

$$\sigma_{i,d,total} = \sqrt{\sigma_{i,model}^2 + \sigma_{i,eve}^2 + \sigma_{j,euv}^2}. \quad (17)$$

448 The total uncertainty is shown in Figure 3c. Since $\sigma_{j,euv}$ ranges from 2.1 to 2.6% as
 449 discussed in Section 3.1, $\sigma_{i,eve}$ dominates the total uncertainty for most wavelengths.

450 Although $\sigma_{i,model}$ tends to be less than 10% for much of the 6-106 nm range, there
 451 are regions where it exceeds 50%. Figure 3a also shows that the uncertainties undergo

452 a marked increase above approximately 92 nm. This is a result of very low measured
453 signal in these wavelength bins as discussed in Section 3.2, and can be seen from Figure
454 3b which shows the uncertainty and irradiance in absolute units for 1 January 2015; the
455 uncertainties are shown with solid color lines and the irradiance is shown with a dashed
456 black line. Here, we see that the uncertainty drops below 10% for the emission lines but
457 becomes large in the inter-line region. Another uncertainty outlier shown in Figure 3c is
458 the bin centered at 63.5 nm. This outlier is from the O V emission line centered at 62.97
459 nm which lies at the boundary of the 62 and 63 nm bins. FISM-M narrows the broad
460 peak of this line observed by SDO EVE, resulting in less irradiance in the 63.5 nm bin.
461 Because the 63-64 nm range is an otherwise low-signal region, this narrowing of the line
462 by the model results in a relatively significant amount of irradiance being removed from
463 this bin; and a net underestimation of the irradiance.

464 4.1.4. FISMv1 Adaptation to Daily Model

465 Outside of the 6-106 nm range, the FISMv1 model was driven with Lyman- α as the
466 proxy above 106 nm and 0.1-7 nm as the proxy below 6 nm. This requires that the SEE
467 XPS 0.1-7 nm irradiance be recalibrated to match the SDO ESP 0.1-7nm channel so that
468 the model coefficients can be used by EUVM which is intercalibrated with SDO ESP
469 as discussed in Section 3.1. This intercalibration adds an additional 10% uncertainty in
470 quadrature to the 0-6 nm values reported by Chamberlin et al. [2007]. Note, no intercal-
471 ibration is required for using the FISMv1 model coefficients with the EUVM Lyman- α
472 proxy because both FISMv1 and EUVM are calibrated against the same (LASP) Lyman- α
473 composite.

4.2. FISM-M Flare Model Description

4.2.1. Flare Model Algorithms

The FISMv1 flare model assumes that all sub-daily fluctuations are attributed to flaring activity, and uses empirical relationships between each 1 nm bin and the GOES XRS 0.1-0.8 nm channel. Similarly, FISM-M uses the 0.1-7 nm EUVM B channel to estimate flare variability at 1 nm resolution based on empirical relationships with 0.1 nm bins. The last two terms on the right-hand side of Equation (7) represent the flaring contribution to the total irradiance, and are written explicitly as

$$\Delta E_{GP,i} = E_i(t) - E_{d,i} \quad (18)$$

and

$$\Delta E_{IP,i} = \frac{d}{dt} (E_i(t) - E_{d,i}) > 0, \quad (19)$$

where we restrict $\Delta E_{IP,i}$ to having irradiance contributions that are greater than 0. These components are modeled by the 0.1-7 nm proxy, P_{0-7} , and its daily minimum, $P_{d,0-7}$, using

$$\Delta E_{GP,i}(t) = C_{GP,i} (P_{0-7}(t) - P_{d,0-7})^{k_{GP,i}}, \quad (20)$$

and

$$\Delta E_{IP,i}(t) = C_{IP,i} \left[\frac{d}{dt} (P_{0-7}(t) - P_{d,0-7}) \right]^{k_{IP,i}}. \quad (21)$$

where the C and k power-law coefficients are found for the i^{th} wavelength bin and SXR proxy, P_{0-7} by the method of least-squares. The derivative in the impulsive phase equa-

487 tions, Equations (19) and (21), is an application of the Neupert Effect, which is the
488 proportionality between the impulsive flare phase and the derivative of the gradual flare
489 phase (Neupert [1968]) and is similar to what was done with FISMv1.

490 4.2.2. Flare Model Calibration

491 FISM-M has been calibrated with 431 flares in the 6-37 nm range and 66 flares in the
492 37-106 nm range measured by SDO EVE. The reason for the reduction in the longer
493 wavelength range is because MEGS B is operated on a reduced duty cycle to preserve the
494 detector which suffers EUV-induced degradation. The calibration set was restricted to
495 M-class and larger flares, because these flares are known to have a measurable impact on
496 the Mars atmosphere (e.g. Thiemann et al. [2015]; Fallows et al. [2015]) and including
497 smaller flares increases the overall uncertainty in the model.

498 Values for $C_{xP,i}$ and $k_{xP,i}$ vary depending on the flare's location on the solar disk for
499 many FISM bins because the emission line dominated 6-106 nm range is more susceptible
500 to resonance scattering within the solar atmosphere than the bremsstrahlung continuum
501 dominated 0-7 nm range (Chamberlin et al. [2008]). This results in the tendency of
502 emissions from flares located closer to the limb, which must propagate through a thicker
503 column of solar atmosphere, to have less EUV content than disk-center flares for the same
504 SXR irradiance. To account for this limb darkening, the calibration set is sub-divided
505 according to disk location, with the *Center*, *Mid* and *Limb -flares* originating from 0°-
506 29°, 30°- 59° and 60°- 90° from disk center, respectively, for the 6-37 nm range. The
507 37-106 nm range was divided into two sub-sets with disk-center flares originating from 0°-
508 59° from disk-center and limb flares originating greater than 60° from disk-center. The
509 smaller sample size for the 37-106 nm range was the reason for using two flare location

510 sub-sets for these bins instead of three. The number of flares in each category is nearly
511 equal, but there is a bias towards more Mid-Flares with 40% in that category and 30% in
512 each of the other two categories.

513 Model coefficients are found independently for each disk location category. In the cur-
514 rent version, the EUVM FISM-M data product through Version 8, Revision 1 did not
515 account for the flare location on the disk because the lack of a solar imaging channel on
516 MAVEN makes estimating flare location difficult. Therefore, the coefficients correspond-
517 ing with the Mid-flare calibration set are used for all flare irradiance estimates. This
518 results in a slight underestimation of disk-center flare irradiance, and a potentially sig-
519 nificant over estimation of limb flare irradiance. An algorithm is described in Section 6
520 to estimate flare location from the EUVM measurements and will be incorporated into
521 FISM-M in the future.

522 Some low signal bins have a minimal flare response, if any at all, and the model fits for
523 these bins are not meaningful. To prevent introducing additional error into the model,
524 these spurious fits are set to zero and the assumption of no flare response for these bins
525 is made. Correlation coefficients are found for disk-center model fits for each bin, and a
526 threshold is set below which the coefficients are set to zero. The threshold was determined
527 by manually inspecting the model fit scatter plots for each bin to find the minimum value
528 of the correlation coefficient that corresponds with scatter plots that show a discernible
529 flare enhancement. Table 2 shows the correlation coefficient threshold and statistical
530 significance for the MEGS A and B channels for the impulsive and gradual model fits.
531 The right-most column shows the number of bins included by the correlation threshold.
532 The correlation coefficient threshold differs between the MEGS channels because of the

533 different sample size of observed flares made by the two channels. Note that every bin
 534 that has an impulsive component also has a gradual-phase component. From Table 2, we
 535 see that many fewer bins have an impulsive phase in addition to the gradual phase.

536 Figure 4 shows example fits of the peak gradual phase irradiance for four bins measured
 537 by MEGS A. The dominant species and the logarithm of its formation temperature are
 538 shown at the top of each panel along with the bin wavelength. The data are split into three
 539 populations according to flare location as discussed above, and a unique fit is found for
 540 each population. There is less scatter evident in the top two panels which correspond with
 541 hotter emissions, and there is less distinction between the center and limb populations
 542 for these hotter emissions. The limb darkening effect is most evident in the bottom right
 543 panel which corresponds with the coolest, and hence lowest height, emission. Here, it is
 544 clear that the center flares tend to have more 30.4 nm irradiance than the limb flares for
 545 the same 0-7 nm irradiance.

546 4.2.3. Flare Model Uncertainty

547 The FISM-M flare model uncertainties are found by first computing the standard devi-
 548 ation of the measurement and fit fractional difference for the impulsive and gradual fits
 549 for each 0.1 nm bin power-law fit in fractional units, $\sigma_{IP,i}$ and $\sigma_{GP,i}$ respectively.

$$\sigma_{IP,i} = \text{stddev} \left(\left[\Delta \vec{E}_{IP,i,model} - \Delta \vec{E}_{IP,i,data} \right] / \Delta \vec{E}_{IP,i,data} \right) \quad (22)$$

$$\sigma_{GP,i} = \text{stddev} \left(\left[\Delta \vec{E}_{GP,i,model} - \Delta \vec{E}_{GP,i,data} \right] / \Delta \vec{E}_{GP,i,data} \right) \quad (23)$$

550 The fractional uncertainty for each bin is found by weighting the impulsive and gradual
 551 phase contributions for each bin,

$$\sigma_{flare,i} = \frac{C_{IP,i} \left(\sigma_{IP,i} \left\langle \frac{d}{dt} (P(t) - P_d(t_d)) \right\rangle \right)^{k_{IP,i}} + C_{GP,i} \left(\sigma_{GP,i} \langle P(t) - P_d(t_d) \rangle \right)^{k_{GP,i}}}{C_{IP,i} \left(\left\langle \frac{d}{dt} (P(t) - P_d(t_d)) \right\rangle \right)^{k_{IP,i}} + C_{GP,i} \left(\langle P(t) - P_d(t_d) \rangle \right)^{k_{GP,i}}}. \quad (24)$$

552 The values for $\sigma_{flare,i}$ are shown in Figure 5a. These values are the 0.1 nm resolution
 553 uncertainty in the flare enhancement above the daily value, and are binned to the j^{th}
 554 1 nm bin using Equation (16). This uncertainty is very large ($>100\%$) in some cases,
 555 reflecting the large scatter in the model fits. The total uncertainty for the 1-minute
 556 cadence FISM-M product is found by adding, in quadrature, the signal-weighted daily
 557 and flare-contribution uncertainties,

$$\sigma_{1-min}(t) = \frac{\sqrt{(\sigma_{flare,j} [\Delta E_{IP}(t) + \Delta E_{GP}(t)])^2 + (\sigma_j E_d)^2}}{E_d + \Delta E_{IP}(t) + \Delta E_{GP}(t)}. \quad (25)$$

558 An example of the time-dependent FISM-M uncertainty for the 1-minute product is shown
 559 in Figure 5, panels b and c for a magnitude X2 (at 1AU) flare observed by MAVEN
 560 EUVM at Mars. Panel b shows the percent uncertainty for the spectrum before the flare
 561 and during the flare peak. Panel c shows an example of the time-dependent uncertainty
 562 for the 13.5 nm and 30.5 nm bins to demonstrate how the uncertainty depends on the
 563 proportion of the total irradiance that occurs due to flares.

564 EUV emissions from lines which form below 10 MK tend to be broader and peak later
 565 than SXR emissions (e.g. Woods et al. [2011], Chamberlin et al. [2012]). This is because
 566 EUV flare line emissions are from hot plasma that is cooling through a line's formation
 567 temperature; and the cooling rate tends to decrease with time (Cargill et al. [1995], Ryan

et al. [2013]). Hence, lines with cooler formation temperatures peak later and decay more slowly. Neither FISM-M nor FISMv1 corrects for this effect and all modeled flare emissions have the same profile as the SXR OP proxy. It is important to note that all reported FISMv1 and FISM-M flare model uncertainties are with respect to the model's ability to estimate the peak flare irradiance. There is additional uncertainty related to the timing of the peak EUV emissions and the total energy deposited that is not currently accounted for in the FISMv1 and FISM-M uncertainty estimates. We cannot give a rigorous characterization of this added uncertainty here, but, qualitatively, EVE data shows the 9.4 nm FeXVIII emission typically peaks hundreds of seconds after the SXR peak, and FWHM values are approximately two times larger for the relatively hot 9.4 nm FeXVIII light curve than the SXR light curve. These effects are exacerbated for cooler emission lines.

4.2.4. FISMv1 Adaptation to Flare Model

For bins outside of the 6-106 nm range, the FISM-M flare component model adjusts the model coefficients of FISMv1 using a cross-calibration of the FISMv1 GOES XRS 0.1-0.8 nm proxy and the FISM-M EUVM 0.1-7 nm proxy. This cross-calibration was implemented by first finding a zero-offset power law relation between the XRS and ESP derived proxies for flare irradiances exceeding $10^{-5}W/m^2$ (M-class) using the method of least squares. The XRS and ESP cross-calibration has associated uncertainties of 55% and 37% for the gradual and impulsive phases, respectively. The conversion from the ESP proxy (either gradual or impulsive), p_e , to the XRS proxy, p_x , is of the form

$$p_{x,j} = m_j \cdot p_{e,j}^{b_j}, \quad (26)$$

589 where $m_I = 0.0324$, $b_I = 1.14$, $m_G = 0.0154$, and $b_G = 1.23$; and the subscript j
 590 corresponds with the impulsive and gradual phases designated by I and G , respectively.

591 The flare irradiance contribution to the i^{th} wavelength bin is of the form

$$\Delta E_i = c_x p_x^{\alpha_x}, \quad (27)$$

592 where the x subscript indicates the values are calibrated for an XRS derived proxy. Equa-
 593 tion (26) can be substituted into (27) to find the model coefficients to be used with p_e
 594 where we use the e subscript to indicate coefficients which are calibrated for an ESP proxy.
 595 Specifically,

$$c_e = c_x \cdot m^{\alpha_x} \quad (28)$$

$$\alpha_e = b \cdot \alpha_x \quad (29)$$

596 where the flare contribution to the irradiance in the i^{th} wavelength bin is now given by

$$E_i = c_e p_e^{\alpha_e}. \quad (30)$$

597 The coefficients for the FISM-M flare model in the wavelength range outside of the
 598 6-106 nm range are found by applying equations 28 and 29 to the FISMv1 flare model
 599 coefficients. The XRS and ESP cross-calibration uncertainty found above is raised to the
 600 power α_e to give the added uncertainties to the model irradiance from cross-calibration
 601 for the gradual and impulsive phases, $\sigma_{G,cross-cal}$ and $\sigma_{I,cross-cal}$, respectively. For bins

602 above 106 nm, $\sigma_{G,cross-cal}$ and $\sigma_{I,cross-cal}$ are approximately 62% and 47%, and below 6
603 nm they are approximately 48% and 32%, respectively.

5. FISM-M Results

5.1. Sample Daily Model Results

604 Sample FISM-M daily model results are shown in Figure 6. Panels a and b show the
605 percent decrease in spectral irradiance at Mars from maximum to minimum values, $(max-$
606 $min)/max \times 100\%$, over solar cycle and solar rotation timescales, respectively. Panel a
607 shows the decrease from perihelion to aphelion observed during the nominal MAVEN
608 mission in black. For comparison, the percent decrease from maximum to minimum of
609 the last solar cycle (23) are shown in red, again taken at Mars. For SC 23, Mars's orbit
610 eccentricity resulted in SC maximum irradiance occurring near perihelion on 12 October
611 2001 and minimum irradiance occurring near aphelion on 25 June 2008. Comparing
612 the two curves shows that, despite the current weak solar cycle, MAVEN was making
613 observations during a period that saw changes in daily average EUV irradiance comparable
614 to what occurred during Solar Cycle 23. However, the spectral decrease is flatter for the
615 period during the MAVEN mission than the preceding solar cycle. This is because much
616 of the difference observed during the MAVEN mission is driven by the changing Mars-
617 Sun distance, which accounts for approximately 40% of the decrease, rather than by solar
618 activity. On the other hand, the spectral dependence of solar activity driven variability
619 causes the structure seen in the Solar Cycle 23 curve. Panel b shows the irradiance
620 decrease due to a single solar rotation occurring in May, 2015. In this case, the variability
621 is almost entirely due to a short term decrease in solar activity because the Mars-Sun
622 distance did not change significantly. This activity dependence causes a more structured

623 spectral decrease, with wavelengths below 30 nm undergoing a 20% decrease over 12 days
624 while wavelengths near 70 nm change by less than 10%.

625 Panel c shows the enhancement in absorbed power per unit volume or, simply, the *power*
626 *density enhancement* from the solar rotation as a function of altitude and wavelength at
627 0.1 nm resolution. To create this figure, a Chapman Production Function, P_c , (Schunk
628 & Nagy [2009]) is computed for each 0.1 nm bin, and the brighter colors correspond with
629 regions of higher ionization per volume of atmosphere (This figure was inspired by an
630 analogous figure for Earth's upper atmosphere in Solomon & Qian [2005]). Specifically,
631 for a given wavelength and altitude bin, P_c is the product of the local solar intensity
632 (in units of power per surface area), neutral gas species densities and their respective
633 ionization cross-sections, gives the power absorbed at that wavelength and altitude. This
634 power density is found for the solar rotation maximum and minimum, and the difference
635 is the power density enhancement. The Mars neutral atmosphere, limited to only CO₂,
636 O, CO, N₂ and O₂, is simulated by the Mars Global Ionosphere-Thermosphere Model
637 (MGITM, Bougher et al. [2015b]) for $L_s = 0$ and F10.7=130 at 27.5° and 2.5° longitude
638 and latitude with respect to the subsolar point. This position is near the MAVEN periapsis
639 for early May, 2015 and the orbital and solar conditions are similar to the actual May,
640 2015 conditions when Mars was near $L_s = 335$ and F10.7 ranged from 101-166. The
641 spectral regions that correspond with the largest power density enhancement are below
642 40 nm, which is densely populated with coronal lines, and the 85-90 nm H continuum
643 region. The EUV enhancement from 17-25 nm and the He II 30.4 nm emission line has
644 a peak deposition near 150 km whereas the EUV enhancement short-ward of 10 nm and

645 between 85 and 90 nm is deposited lower in the atmosphere, near 130 km due to the
646 ionization cross-sections decreasing with wavelength.

5.2. Flare Model Sample Results

647 Figure 7 shows example results for fifteen 1 nm bins from FISM-M run at Earth (and
648 driven with the CAL proxies) in red compared with SDO EVE data in black for 15
649 February 2011 which includes an X2.2 flare near 02:00 UT. The bin wavelength in nm is
650 shown above each panel. FISM-M and SDO EVE are in relatively good agreement for the
651 X2.2 flare during the rising phase and flare peak, but FISM-M under predicts the duration
652 of the decay phase for some lines (e.g. 28.5 nm and 33.5 nm) as discussed in Section 4.2.3.
653 The 28.5 nm bin shows a substantial increase in irradiance near 12:00 UT not captured
654 by FISM-M. This demonstrates the limitations of FISM-M for modeling non-flaring sub-
655 daily irradiance. The feature does not appear in the FISM-M output because it did not
656 appear in the 0.1-7 nm data, likely because it was due to an event that heated plasma
657 to the formation temperature of Fe XII, which dominates the 28.5 nm bin, but not to
658 temperatures that result in significant SXR emissions.

659 Figure 8 shows FISM-M results for 3 test flares with magnitudes C5, M5 and X1 at
660 Mars. Note the magnitude ratings are with respect to 1 AU. The spectral irradiance is
661 shown in Panel a and modeled for Mars on 1 January 2015. Panel b shows the percent
662 of the daily average for the peak of each flare on the same day. The increase of 6-106
663 nm integrated irradiance is 2.5%, 9.4% and 14.7% larger than the 1 January 2015 daily
664 average for the C5, M5, and X1 flares, respectively. From Panel a, we see that the 30.5 nm
665 bin, which includes the bright He II 30.4 nm line, has the highest peak flare contribution,
666 followed by the 1.5 nm SXR bin. From Panel b, we see that the 0.5 nm SXR bin shows

667 the largest percent increase. This increase is rivaled by the 9.5-13.5 spectral region which
668 contains many emissions from highly ionized Fe. This same region and its neighboring
669 bins show a distinct enhancement feature in Panel a. Panel c shows the X1 flare power
670 density enhancement as a function of wavelength and altitude using the same reference
671 atmosphere discussed in Section 5.1. Here, we see the most intense increase occurs near
672 120 km due to the SXR, and these wavelengths show a significant enhancement which
673 extends upwards to 200 km. The He II 30.4 nm enhancement is deposited somewhat
674 higher with a peak near 150 km, and the 9-15 nm enhancement peaks near 135 km.
675 Above 97.3 nm, the EUV emissions penetrate deeper into the atmosphere because the
676 more tenuous O₂ is the only major species with finite ionization cross-sections at these
677 longer wavelengths.

6. FISM-M Future Improvements

678 Future versions of the EUVM FISM-M data product should have improvements that
679 correct for some of the known deficiencies stated above. We briefly discuss four high
680 priority improvements that will be implemented in the coming year.

681 As discussed in Section 4.2, limb flares tend to have a reduced EUV spectral content
682 when compared to disk-center flares for the same SXR irradiance; and distinct sets of
683 model coefficients are found to correspond to different flare locations. FISMv1 accounts
684 for flare location by using information derived from Earth based solar x-ray imagers un-
685 available to FISM-M when a flare is not visible from Earth. Therefore, FISM-M must
686 estimate the flare location without imaging observations to locate a flare. We propose an
687 algorithm for coarse flare location based on the relative intensities of the optically thin
688 EUVM Level 2 0.1-7 nm and optically thick Lyman- α measurements. Figure 9 shows

689 scatter plots of Earth measured 0.1-7 nm and 121.6 nm peak flare irradiances made by
690 SDO ESP and the GOES EUV Sensor E (EUVS-E) channel (Viereck et al. [2007]). They
691 have been sorted into two populations, those originating inside and those originating out-
692 side of 45° of disk-center. Power law fits that predict the Lyman- α irradiance for a given
693 0.1-7 nm irradiance are found for each population and are over-plotted. These curves,
694 with equations shown in the legend, partition the scatter plot into three regions that are
695 designated 'Center', 'Mid' and 'Limb'. Relative peak flare intensities measured by EUVM
696 will be programmatically compared with these curves to estimate the flare location, and
697 the appropriate set of location-dependent FISM-M flare coefficients will be applied.

698 A second improvement involves modeling non-flaring sub-daily variability. FISM-M cur-
699 rently predicts daily average irradiance and flaring EUV irradiance, but does not predict
700 non-flaring sub-daily variability. This is because the EUVM 17-22 nm channel also has
701 a SXR component that must be removed, and this is done through filtering over daily
702 time-scales because it is ambiguous whether sample-to-sample variability is from a change
703 in the 17-22 nm band or the SXR contribution. Therefore, the FISM-M daily (non-flaring)
704 model cannot simply be implemented at a higher time cadence as a minutely non-flaring
705 component. However, the SXR contribution to the EUVM 17-22 nm channel can be suit-
706 ably removed at the time-scales of an orbit average. This will then be interpolated to a
707 higher time-cadence and used to estimate a non-flaring component in future versions of
708 the EUVM FISM-M data product.

709 A third improvement will reduce uncertainty in impulsive and transition region flare
710 emissions by using the Lyman- α channel in addition to the nominal 0.1-7 nm channel
711 for the FISM-M flare component. The intense He II 30.4 nm flare emission is a partic-

ular example where using Lyman- α as a flare proxy will likely reduce the flare model uncertainty because the two emissions originate from similar regions in the Sun's atmosphere. An added benefit of using this emission as a proxy for emissions that show flare limb-darkening is that using the flare location to correct for this effect may become unnecessary because the Lyman- α flare proxy limb-darkens. This should inherently account for the limb-darkening effect in modeled emissions derived from it.

A fourth improvement will correct for the broadening and peak-delay seen in EUV emission lines when compared to SXR emissions. Thiemann [2016b] showed that a single-pole low pass filter with the appropriate time constant will modulate SXR solar flare light curves to match those of EUV emissions. This technique will be applied to future versions of the MAVEN EUVM FISM-M data product.

7. Summary and Conclusions

FISM-M reproduces daily average irradiance calibrated against SDO EVE observations in the 6-106 nm range by using the EUVM measurements as proxies for solar spectral irradiance variability. The model uncertainty in this range for daily averaged irradiance is less than 5% for most wavelength bins, and the larger total uncertainty is largely driven by the uncertainty in the data-sets used to calibrate the model. Uncertainties during flares depend on the size of the flare and increase as the flare contribution becomes larger; sample X2 flare irradiances are below approximately 50% for most 1 nm model bins. FISM-M predicts the average peak EUV flare irradiance measured by SDO/EVE for a given SXR irradiance. We find that the 6-106 nm irradiance increases by 2.5%, 9.4% and 14.7% for C5, M5 and X1 flares respectively.

733 We presented examples of EUV variability observed during the MAVEN primary mis-
734 sion. We showed that the maximum change in irradiance below 50 nm observed during
735 the primary MAVEN mission is approximately 50% smaller than variations over the past
736 two solar cycles due in part to the relative weakness of the observed solar maximum and
737 the fact that the observations during Mars aphelion occurred during relative moderate
738 solar conditions. We expect the maximum observed change will increase when MAVEN
739 makes measurements at Mars during the coming aphelion when solar activity is expected
740 to be nearer minimum levels. We also showed that the enhanced EUV power density in
741 the Mars atmosphere is comparable during the strong solar rotation of May, 2015 and a
742 hypothetical X1 flare. Early MAVEN results reported changes to the Mars atmosphere in
743 the past due to both of these phenomena (e.g. Forbes et al. [2006] and Thiemann et al.
744 [2015]) and FISM-M spectra can be used to better characterize these changes.

745 The availability of high time cadence EUV spectra for the MAVEN mission should
746 improve the quality of science enabled by the MAVEN mission by capturing the full
747 structure and variability of EUV irradiance; reducing the uncertainty associated with
748 using Earth-derived spectra and activity indices as was necessary prior to the arrival of
749 MAVEN at Mars.

750 **Acknowledgments.** This work has been funded by the NASA MAVEN mis-
751 sion, Contract Number NNH10CC04C. E.M.B.T. thanks Dr. S. Xu for provid-
752 ing the ionization cross-sections used for calculating atmospheric power density spec-
753 tra. E.M.B.T. also thanks the anonymous reviewers for their thorough feedback
754 which resulted in an improved paper. All EUVM datasets used in this paper
755 are available through the NASA Planetary Data System (PDS). All datacubes con-

756 taining the M-GITM model neutral densities used in this paper are available on
757 the public version of the MAVEN Science Data Center (SDC) website at LASP
758 (<https://lasp.colorado.edu/maven/sdc/public/pages/models.html>). FISM-M model coef-
759 ficients were submitted as Supporting Information for this article and are archived by AGU
760 Journals for use by other scientists. Portions of the work used the CHIANTI Atomic
761 Database; CHIANTI is a collaborative project involving George Mason University, the
762 University of Michigan (USA) and the University of Cambridge (UK).

References

- 763 Aschwanden, M. *Physics of the solar corona: an introduction with problems and solutions*.
764 Springer Science & Business Media, 2006.
- 765 Bornmann, P. L., Speich, D., Hirman, J., Matheson, L., Grubb, R., Garcia, H. A., &
766 Viereck, R. GOES X-ray sensor and its use in predicting solar-terrestrial disturbances.
767 In *SPIE's 1996 International Symposium on Optical Science, Engineering, and Instru-*
768 *mentation*, pages 291–298. International Society for Optics and Photonics, 1996.
- 769 Bougher, S. W., Roeten, K., Olsen, K., Mahaffy, P. R., Benna, M., Elrod, M., Jain, S.,
770 Schneider, N. M., Deighan, J., Thiemann, E., et al. The structure and variability of
771 Mars dayside thermosphere from MAVEN NGIMS and IUVS measurements: Seasonal
772 and solar activity trends in scale heights and temperatures. *Journal of Geophysical*
773 *Research: Space Physics*, 2016.
- 774 Bougher, S., Cravens, T., Grebowsky, J., & Luhmann, J. The aeronomy of Mars: Charac-
775 terization by MAVEN of the upper atmosphere reservoir that regulates volatile escape.
776 *Space Science Reviews*, 195(1-4):423–456, 2015a.

- 777 Bougher, S., Pawlowski, D., Bell, J., Nelli, S., McDunn, T., Murphy, J., Chizek, M., &
778 Ridley, A. Mars Global Ionosphere-Thermosphere Model: Solar cycle, seasonal, and
779 diurnal variations of the Mars upper atmosphere. *Journal of Geophysical Research:*
780 *Planets*, 120(2):311–342, 2015b.
- 781 Cargill, P. J., Mariska, J. T., & Antiochos, S. K. Cooling of solar flares plasmas. 1:
782 Theoretical considerations. *The Astrophysical Journal*, 439:1034–1043, 1995.
- 783 Carr, M. H. & Head, J. W. Oceans on Mars: An assessment of the observational evidence
784 and possible fate. *Journal of Geophysical Research: Planets*, 108(E5), 2003.
- 785 Carrington, R. C. On the distribution of the solar spots in latitudes since the beginning
786 of the year 1854, with a map. *Monthly Notices of the Royal Astronomical Society*, 19:
787 1–3, 1858.
- 788 Chaffin, M. S., Chaufray, J.-Y., Deighan, J., Schneider, N. M., McClintock, W. E., Stewart,
789 A. I. F., Thiemann, E., Clarke, J. T., Holsclaw, G. M., Jain, S. K., et al. Three-
790 dimensional structure in the Mars H corona revealed by IUVS on MAVEN. *Geophysical*
791 *Research Letters*, 42(21):9001–9008, 2015.
- 792 Chamberlin, P., Milligan, R., & Woods, T. Thermal evolution and radiative output of
793 solar flares observed by the EUV variability experiment (EVE). *Solar Physics*, 279(1):
794 23–42, 2012.
- 795 Chamberlin, P. C., Woods, T. N., & Eparvier, F. G. Flare irradiance spectral model
796 (FISM): Daily component algorithms and results. *Space Weather*, 5(7), 2007.
- 797 Chamberlin, P. C., Woods, T. N., & Eparvier, F. G. Flare irradiance spectral model
798 (FISM): Flare component algorithms and results. *Space Weather*, 6(5), 2008.

- 799 Chassefière, E. & Leblanc, F. Mars atmospheric escape and evolution; interaction with
800 the solar wind. *Planetary and Space Science*, 52(11):1039–1058, 2004.
- 801 Chaufray, J.-Y., Deighan, J., Chaffin, M. S., Schneider, N. M., McClintock, W. E., Stewart,
802 A. I. F., Jain, S. K., Crismani, M., Stiepen, A., Holsclaw, G. M., et al. Study of the
803 Martian cold oxygen corona from the O I 130.4 nm by IUVS/MAVEN. *Geophysical
804 Research Letters*, 42(21):9031–9039, 2015.
- 805 Deighan, J., Chaffin, M., Chaufray, J.-Y., Stewart, A. I. F., Schneider, N., Jain, S. K.,
806 Stiepen, A., Crismani, M., McClintock, W. E., Clarke, J. T., et al. MAVEN IUVS
807 observation of the hot oxygen corona at Mars. *Geophysical Research Letters*, 42(21):
808 9009–9014, 2015.
- 809 Didkovsky, L., Judge, D., Wieman, S., Woods, T., & Jones, A. EUV spectrophotometer
810 (ESP) in extreme ultraviolet variability experiment (EVE): Algorithms and calibrations.
811 In *The Solar Dynamics Observatory*, pages 179–205. Springer, 2012.
- 812 Eparvier, F., Chamberlin, P., Woods, T., & Thiemann, E. The solar extreme ultraviolet
813 monitor for MAVEN. *Space Science Reviews*, 195(1-4):293–301, 2015.
- 814 Evans, J. S., Stevens, M. H., Lumpe, J., Schneider, N. M., Stewart, A. I. F., Deighan,
815 J., Jain, S. K., Chaffin, M. S., Crismani, M., Stiepen, A., et al. Retrieval of CO₂
816 and N₂ in the Martian thermosphere using dayglow observations by IUVS on MAVEN.
817 *Geophysical Research Letters*, 42(21):9040–9049, 2015.
- 818 Fallows, K., Withers, P., & Gonzalez, G. Response of the Mars ionosphere to solar
819 flares: Analysis of MGS radio occultation data. *Journal of Geophysical Research: Space
820 Physics*, 120(11):9805–9825, 2015.

- 821 Forbes, J., Bruinsma, S., Lemoine, F., Bowman, B., & Konopliv, A. Variability of the
822 Satellite Drag Environments of Earth, Mars and Venus due to Rotation of the Sun. In
823 *AGU Fall Meeting Abstracts*, volume 1, page 04, 2006.
- 824 Haider, S. & Mahajan, K. Lower and upper ionosphere of Mars. *Space Science Reviews*,
825 182(1-4):19–84, 2014.
- 826 Hinteregger, H. E., Fukui, K., & Gilson, B. R. Observational, reference and model data
827 on solar EUV, from measurements on AE-E. *Geophysical Research Letters*, 8(11):1147–
828 1150, 1981.
- 829 Hock, R., Chamberlin, P., Woods, T., Crotser, D., Eparvier, F., Woodraska, D., & Woods,
830 E. Extreme ultraviolet variability experiment (EVE) multiple EUV grating spectro-
831 graphs (MEGS): radiometric calibrations and results. *Solar Physics*, 275(1-2):145–178,
832 2012.
- 833 Jain, S. K., Stewart, A. I. F., Schneider, N. M., Deighan, J., Stiepen, A., Evans, J. S.,
834 Stevens, M. H., Chaffin, M. S., Crismani, M., McClintock, W. E., et al. The structure and
835 variability of Mars upper atmosphere as seen in MAVEN/IUVS dayglow observations.
836 *Geophysical Research Letters*, 42(21):9023–9030, 2015.
- 837 Jakosky, B. M. & Phillips, R. J. Mars' volatile and climate history. *nature*, 412(6843):
838 237–244, 2001.
- 839 Jakosky, B. M., Lin, R., Grebowsky, J., Luhmann, J., Mitchell, D., Beutelschies, G.,
840 Priser, T., Acuna, M., Andersson, L., Baird, D., et al. The Mars atmosphere and
841 volatile evolution (MAVEN) mission. *Space Science Reviews*, 195(1-4):3–48, 2015.
- 842 Landi, E., Del Zanna, G., Young, P., Dere, K., & Mason, H. CHIANTI?An atomic
843 database for emission lines. XII. Version 7 of the database. *The Astrophysical Journal*,

- 844 744(2):99, 2011.
- 845 Lean, J. THE SUN'S VARIABLE RADIATION AND ITS RELEVANCE FOR EARTH
846 1. *Annual Review of Astronomy and Astrophysics*, 35(1):33–67, 1997.
- 847 McClintock, W. E., Rottman, G. J., & Woods, T. N. SOLar Stellar Irradiance Comparison
848 Experiment II (SOLSTICE II) for the NASA Earth Observing System's Solar Radiation
849 and Climate Experiment Mission. In *International Symposium on Optical Science and
850 Technology*, pages 225–234. International Society for Optics and Photonics, 2000.
- 851 Neupert, W. M. Comparison of solar X-ray line emission with microwave emission during
852 flares. *The Astrophysical Journal*, 153:L59, 1968.
- 853 Peterson, W., Thiemann, E., Eparvier, F. G., Andersson, L., Fowler, C., Larson, D.,
854 Mitchell, D., Mazelle, C., Fontenla, J., Evans, J. S., et al. Photoelectrons and so-
855 lar ionizing radiation at Mars: Predictions versus MAVEN observations. *Journal of
856 Geophysical Research: Space Physics*, 121(9):8859–8870, 2016.
- 857 Phillips, K. J., Feldman, U., & Landi, E. *Ultraviolet and X-ray Spectroscopy of the Solar
858 Atmosphere*, volume 44. Cambridge University Press Cambridge, 2008.
- 859 Rahmati, A., Larson, D., Cravens, T., Lillis, R., Dunn, P., Halekas, J., Connerney, J.,
860 Eparvier, F., Thiemann, E., & Jakosky, B. MAVEN insights into oxygen pickup ions
861 at Mars. *Geophysical Research Letters*, 42(21):8870–8876, 2015.
- 862 Richards, P., Fennelly, J., & Torr, D. EUVAC: A solar EUV flux model for aeronomic
863 calculations. *Journal of Geophysical Research: Space Physics*, 99(A5):8981–8992, 1994.
- 864 Richards, P. G., Woods, T. N., & Peterson, W. K. HEUVAC: A new high resolution solar
865 EUV proxy model. *Advances in space research*, 37(2):315–322, 2006.

- 866 Ryan, D. F., Chamberlin, P. C., Milligan, R. O., & Gallagher, P. T. Decay-phase cooling
867 and inferred heating of M-and X-class solar flares. *The Astrophysical Journal*, 778(1):
868 68, 2013.
- 869 Sakai, S., Andersson, L., Cravens, T. E., Mitchell, D. L., Mazelle, C., Rahmati, A., Fowler,
870 C. M., Bougher, S. W., Thiemann, E., Eparvier, F. G., et al. Electron energetics in
871 the Martian dayside ionosphere: Model comparisons with MAVEN data. *Journal of*
872 *Geophysical Research: Space Physics*, 121(7):7049–7066, 2016.
- 873 Schunk, R. & Nagy, A. *Ionospheres: physics, plasma physics, and chemistry*. Cambridge
874 university press, 2009.
- 875 Snow, M., Weber, M., Machol, J., Viereck, R., & Richard, E. Comparison of Magnesium II
876 core-to-wing ratio observations during solar minimum 23/24. *Journal of Space Weather*
877 *and Space Climate*, 4:A04, 2014.
- 878 Solomon, S. C. & Qian, L. Solar extreme-ultraviolet irradiance for general circulation
879 models. *Journal of Geophysical Research: Space Physics*, 110(A10), 2005.
- 880 Thiemann, E. *Multi-Spectral Sensor Driven Solar EUV Irradiance Models with Improved*
881 *Spectro-Temporal Resolution for Space Weather Applications at Earth and Mars*. PhD
882 thesis, UNIVERSITY OF COLORADO AT BOULDER, 2016a.
- 883 Thiemann, E. A New Relationship Between Soft X-Rays and EUV Flare Light Curves.
884 In *AAS/Solar Physics Division Meeting*, volume 47, 2016b.
- 885 Thiemann, E., Eparvier, F., Andersson, L., Fowler, C., Peterson, W., Mahaffy, P., Eng-
886 land, S., Larson, D., Lo, D., Schneider, N., et al. Neutral density response to solar flares
887 at Mars. *Geophysical Research Letters*, 42(21):8986–8992, 2015.

- 888 Thuillier, G., Bolsée, D., Schmidtke, G., Foujols, T., Nikutowski, B., Shapiro, A., Brunner,
889 R., Weber, M., Erhardt, C., Hersé, M., et al. The solar irradiance spectrum at solar
890 activity minimum between solar cycles 23 and 24. *Solar Physics*, 289(6):1931–1958,
891 2014.
- 892 Tobiska, W. K. & Eparvier, F. EUV97: Improvements to EUV irradiance modeling in
893 the soft X-rays and FUV. In *Solar Electromagnetic Radiation Study for Solar Cycle 22*,
894 pages 147–159. Springer, 1998.
- 895 Tobiska, W. K., Woods, T., Eparvier, F., Viereck, R., Floyd, L., Bouwer, D., Rottman,
896 G., & White, O. The SOLAR2000 empirical solar irradiance model and forecast tool.
897 *Journal of Atmospheric and Solar-Terrestrial Physics*, 62(14):1233–1250, 2000.
- 898 Viereck, R., Hanser, F., Wise, J., Guha, S., Jones, A., McMullin, D., Plunket, S., Strick-
899 land, D., & Evans, S. Solar extreme ultraviolet irradiance observations from GOES:
900 design characteristics and initial performance. In *Optical Engineering+ Applications*,
901 pages 66890K–66890K. International Society for Optics and Photonics, 2007.
- 902 Von Storch, H. & Zwiers, F. W. *Statistical analysis in climate research*. Cambridge
903 university press, 2001.
- 904 Woods, T. N., Bailey, S., Eparvier, F., Lawrence, G., Lean, J., McClintock, B., Roble,
905 R., Rottman, G. J., Solomon, S. C., Tobiska, W. K., et al. TIMED solar EUV experi-
906 ment. *Physics and Chemistry of the Earth, Part C: Solar, Terrestrial & Planetary*
907 *Science*, 25(5):393–396, 2000.
- 908 Woods, T. N., Eparvier, F. G., Bailey, S. M., Chamberlin, P. C., Lean, J., Rottman, G. J.,
909 Solomon, S. C., Tobiska, W. K., & Woodraska, D. L. Solar EUV Experiment (SEE):
910 Mission overview and first results. *Journal of Geophysical Research: Space Physics*, 110

- 911 (A1), 2005.
- 912 Woods, T. N., Hock, R., Eparvier, F., Jones, A. R., Chamberlin, P. C., Klimchuk, J. A.,
913 Didkovsky, L., Judge, D., Mariska, J., Warren, H., et al. New solar extreme-ultraviolet
914 irradiance observations during flares. *The Astrophysical Journal*, 739(2):59, 2011.
- 915 Woods, T. N., Snow, M., Harder, J., Chapman, G., & Cookson, A. A Different View of
916 Solar Spectral Irradiance Variations: Modeling Total Energy over Six-Month Intervals.
917 *Solar Physics*, 290(10):2649–2676, 2015.
- 918 Woods, T., Eparvier, F., Hock, R., Jones, A., Woodraska, D., Judge, D., Didkovsky, L.,
919 Lean, J., Mariska, J., Warren, H., et al. Extreme ultraviolet variability experiment
920 (EVE) on the solar dynamics observatory (SDO): overview of science objectives, instru-
921 ment design, data products, and model developments. *Solar Physics*, 275(1-2):115–143,
922 2012.

References

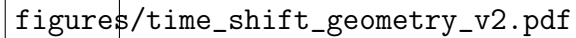


Figure 1. a and b) Geometric definitions used to interpolate Earth measured irradiance proxies to the Mars angular position. t_d is the day when irradiance is needed at Mars. It is found by linearly interpolating irradiance at Earth measured on days $t_d - \Delta t_1$ and $t_d + \Delta t_2$. c) The Mars-Sun-Earth angle and d) the Mars-Sun distance squared as a function of time during the MAVEN mission. See Section 2 for details.

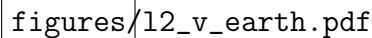


Figure 2. Panels a, c and d show measurements made by MAVEN EUVM in thick red and measurements from comparable channels located at Earth in thin blue. The Earth measurements are scaled to $R_M(t)$. Panels b, d and f are scatterplots of 81 day running averages of the comparable EUVM and Earth-based measurements scaled to 1 AU with the 1:1 line shown, and the standard deviations from the 1:1 line are given on each panel in %.

Table 1. Earth/EUVM Cross-Calibrated Channels Used to drive FISM-M. The Earth channel serves as a secondary operational proxy when the EUVM data are unavailable. The Tertiary OP proxy is used if the Primary OP and Secondary OP proxies are unavailable.

Primary OP Proxy	CAL & Secondary OP Proxy	SORCE & SEE Era CAL Proxy	Tertiary OP Proxy
L2 0.1-7 nm	SDO/ESP v5 0.1-7 nm	SEE/XPS v11 Ti	L2 17-22 nm
L2 17-22 nm	SDO/ESP v5 17-22 nm	None	L2 121.6 nm
L2 121.6 nm	LASP Lyman- α Composite*	LASP Lyman- α Composite*	Mg II c/w
Mg II c/w**		N/A	F10.7

*Scaled by 1.04 to agree with SORCE SOLSTICE. See text for details. **Only used when Primary L2 and Secondary OP proxies are unavailable.

figures/proxy_unc.pdf

Figure 3. Uncertainties found by comparing FISM-M with SDO EVE measurements. a) Percent uncertainty for each 0.1 nm bin predicted by the three EUVM proxies. The triangles correspond with bins where the F-test found the differences between the smallest and second-smallest uncertainties are statistically insignificant. b) Absolute uncertainty is shown in color and the FISM-M minimum irradiance spectrum is over-plotted with a black dashed line. The values are scaled to 1AU. c) 1 nm signal weighted uncertainty using the minimum model uncertainty for each bin shown in panels a and b. The model and total uncertainties are shown the with black and dashed lines, respectively.

Table 2. Correlation coefficient thresholds for zeroing out spurious model fits.

Range/Phase	Correlation	Sample Size	Likelihood Unrelated	Bins Included
6-36 nm/GP	0.45	129	0.06%	186
37-106 nm/GP	0.3	46	4.2%	460
6-36 nm/IP	0.45	129	0.06%	16
37-106 nm/IP	0.3	46	4.2%	22

figures/13_megs_a_GP_ex.pdf

Figure 4. Example bins for the FISM-M gradual-phase fits from MEGS-A. The species, wavelength and Log formation temperature are given at the top of each panel. Power-law fits are found between the MEGS (vertical axis) and the ESP 0-7 nm (horizontal axis) measured peak gradual phase irradiance. The symbols and colors corresponds with flare location on the disk as discussed in the text, and best fit for each population is shown.

figures/13_flr_unc_panel.pdf

Figure 5. FISM-M flare uncertainty. a) The fractional uncertainty for the flare model. Note that this is not the sub-daily model uncertainty because the flare contribution is a fraction of the total irradiance and the uncertainties must be weighted accordingly. Panels b and c correspond with an X2 flare observed by EUVM. b) Spectrum uncertainty for flare and pre-flare. The uncertainty increases as the proportion of the total irradiance from the flare increases. c) Example time-dependent uncertainties for the 30.5 nm and 13.5 nm bins.

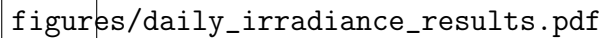


Figure 6. Example results for the FISM-M daily model. Panel a shows the percent decrease from maximum at perihelion to minimum at aphelion during the MAVEN mission in black and solar cycle 23 in red for comparison. Panel b shows the percent decrease from maximum to minimum during a single solar rotation observed in May 2015. Panel c shows the ionization enhancement in the Mars atmosphere due to solar rotation.

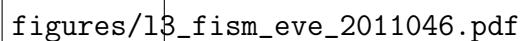


Figure 7. FISM-M run at Earth compared against SDO/EVE for year-day 2011046.

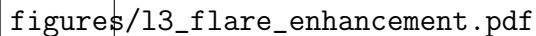


Figure 8. Example FISM-M flare results for magnitude C5, M5 and X1 flares from 0.1-106 nm. Panel a shows the peak flare irradiance at Mars on 1 January 2015, and Panel b shows the enhancement over the daily average. Panel c shows where in the Mars atmosphere the irradiance enhancement from an X1 flare is deposited.

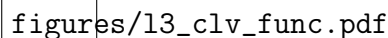
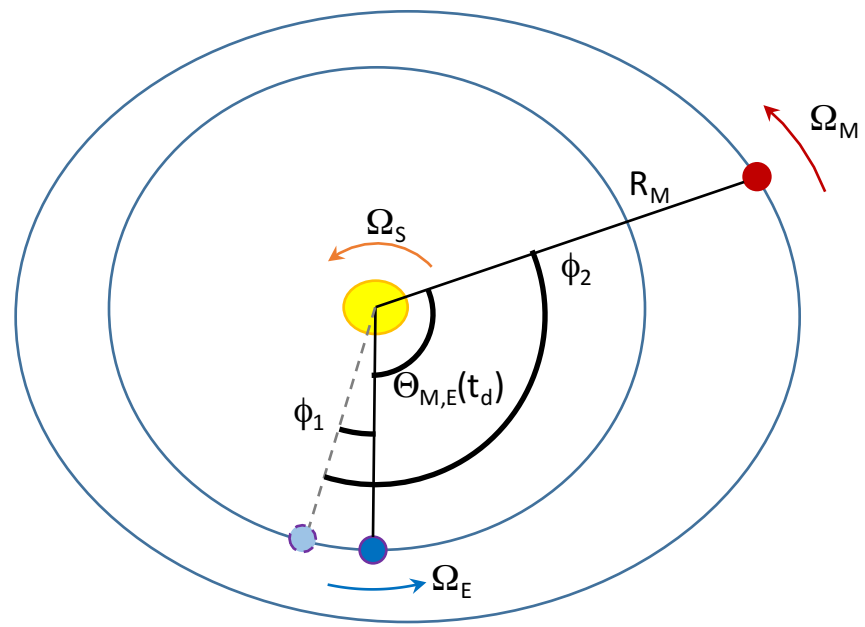


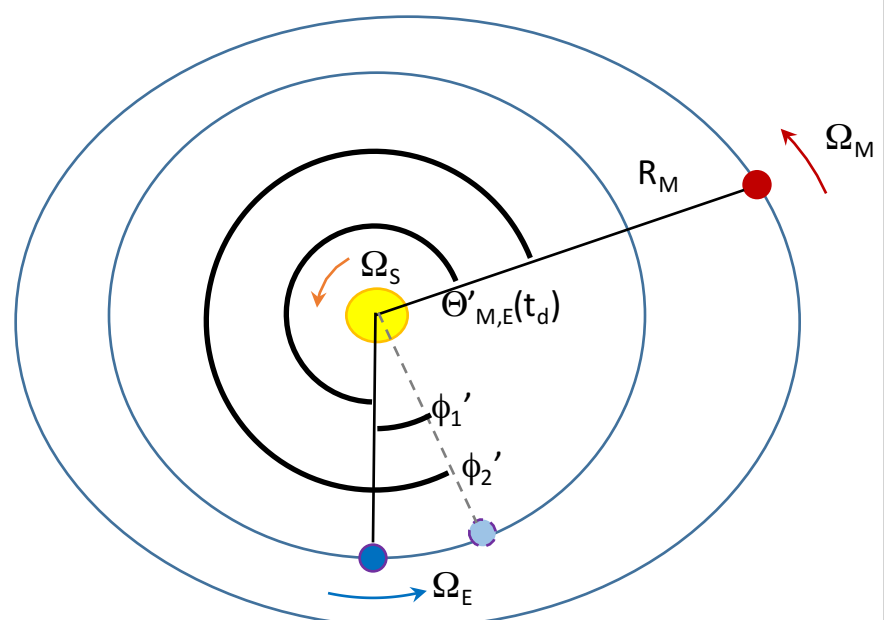
Figure 9. Data and curves used to determine flare location based on the relative response of the EUVM Lyman- α and 0.1-7 nm channels. Fits are found of the training set flares with a 0.1-7 nm signal above 1 mW/m^2 for those within 45° from center and those outside of 45° from center. These curves are taken to the boundaries between Center, Mid and Limb flares. Source data to determine this relation are from the ESP 0.1-7 nm and GOES-15 EUVS-E Lyman- α channels.

a.



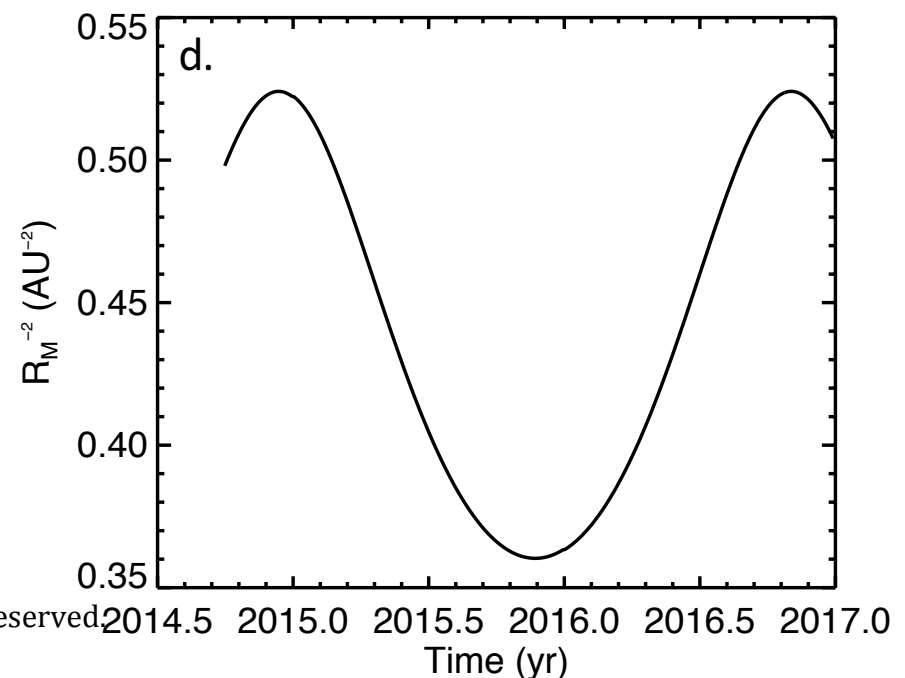
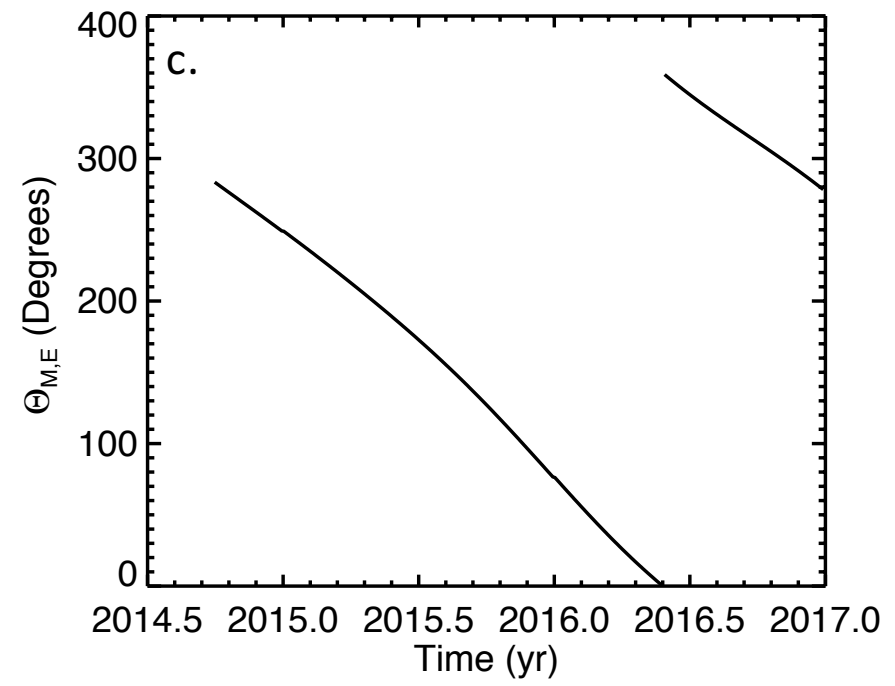
Not to scale.

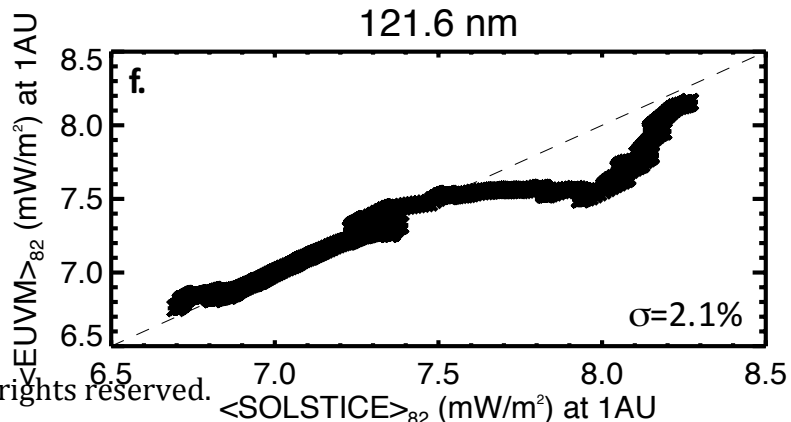
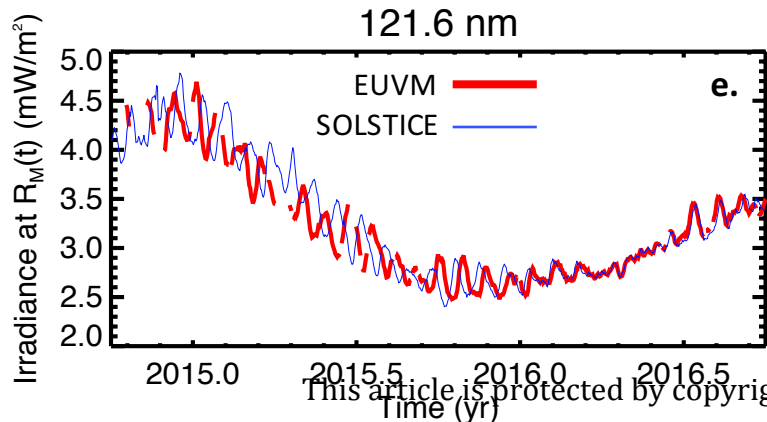
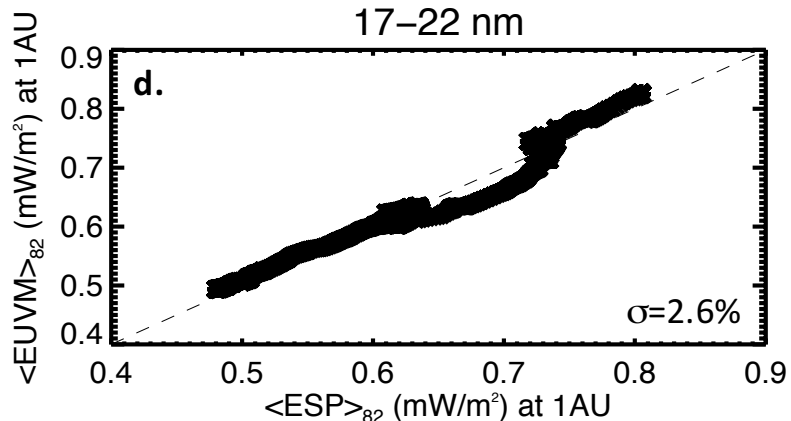
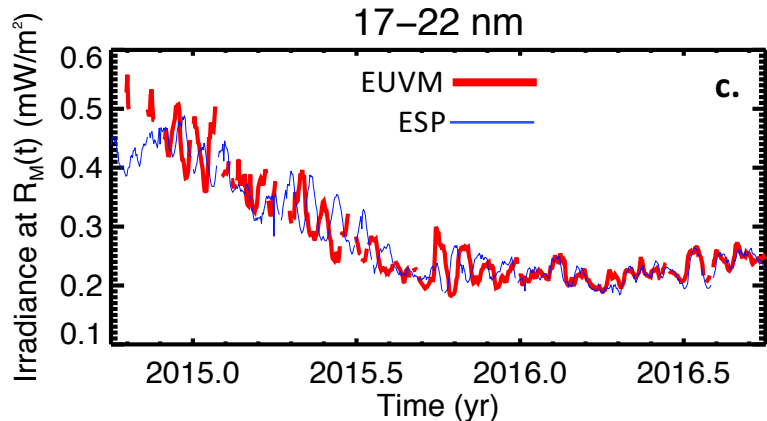
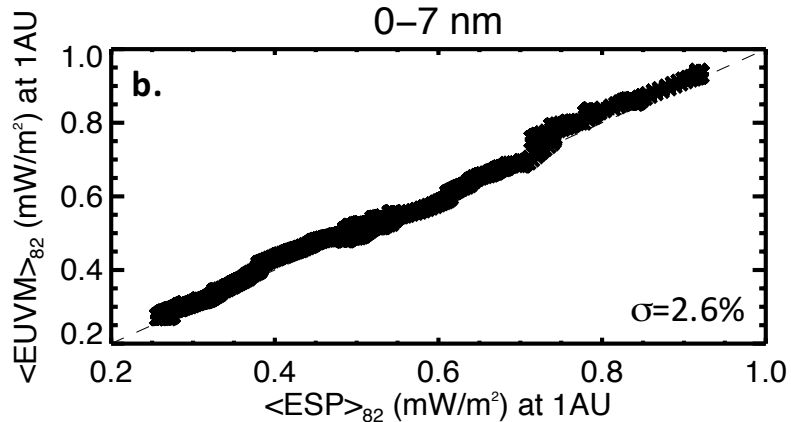
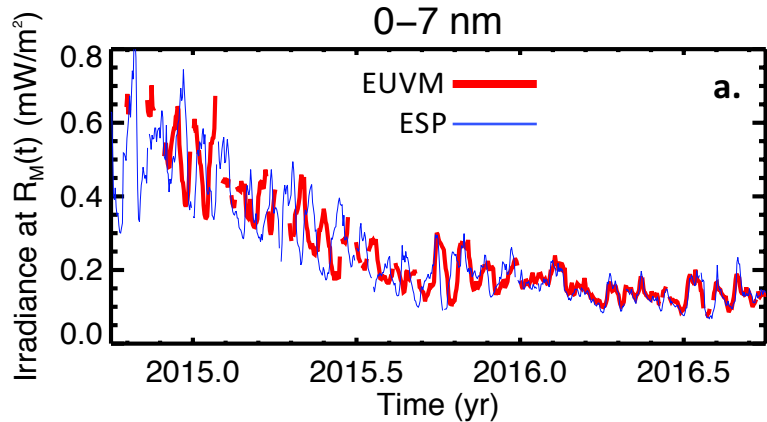
b.



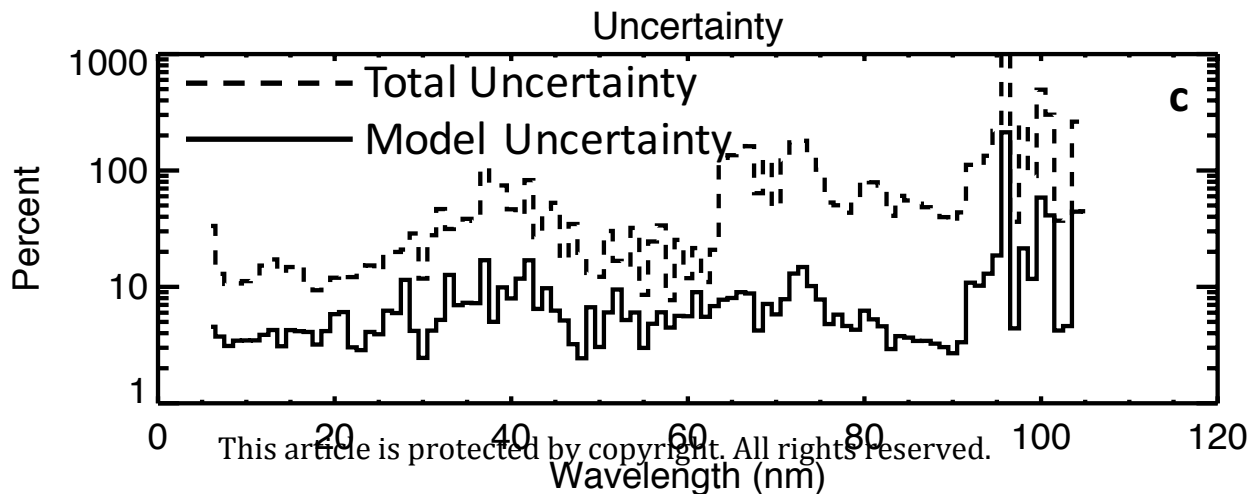
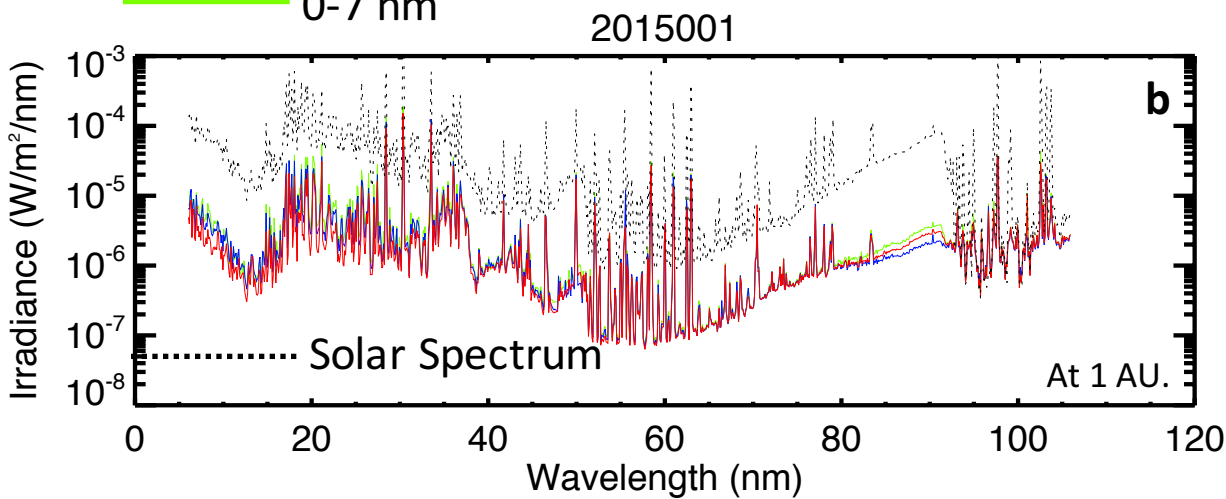
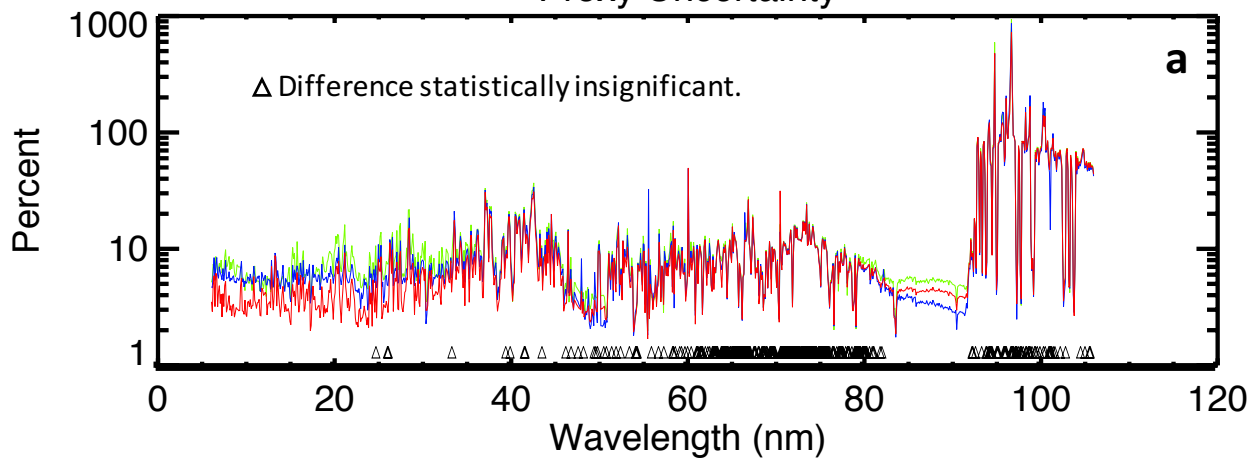
Not to scale.

This article is protected by copyright. All rights reserved





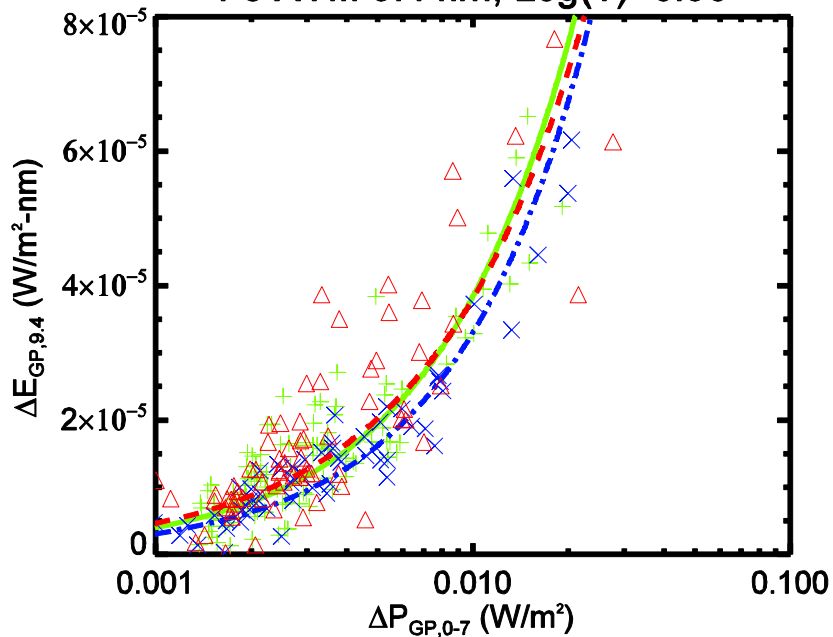
Proxy Uncertainty



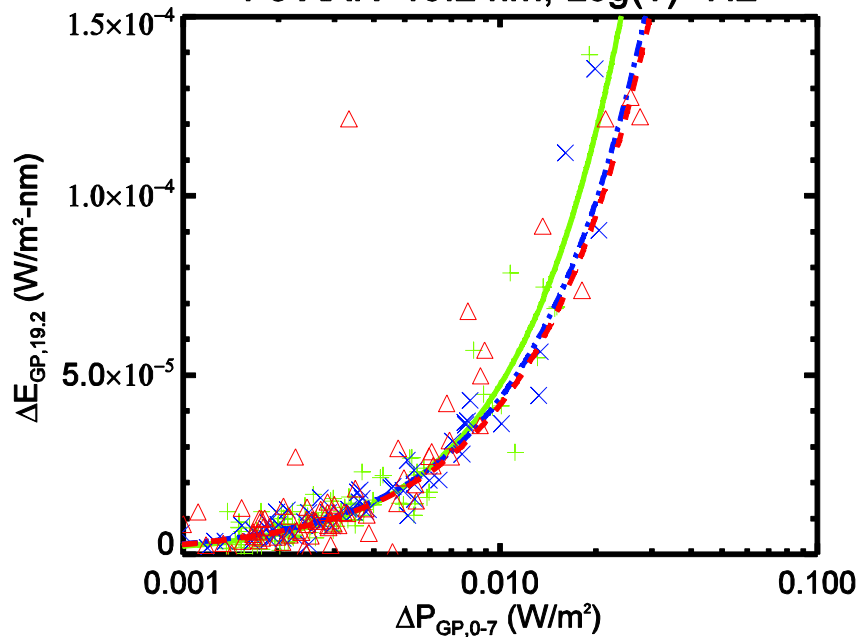
× Center-Flare Data
+ Mid-Flare Data
△ Limb-Flare Data

--- Center-Flare Model
— Mid-Flare Model
- - - Limb-Flare Model

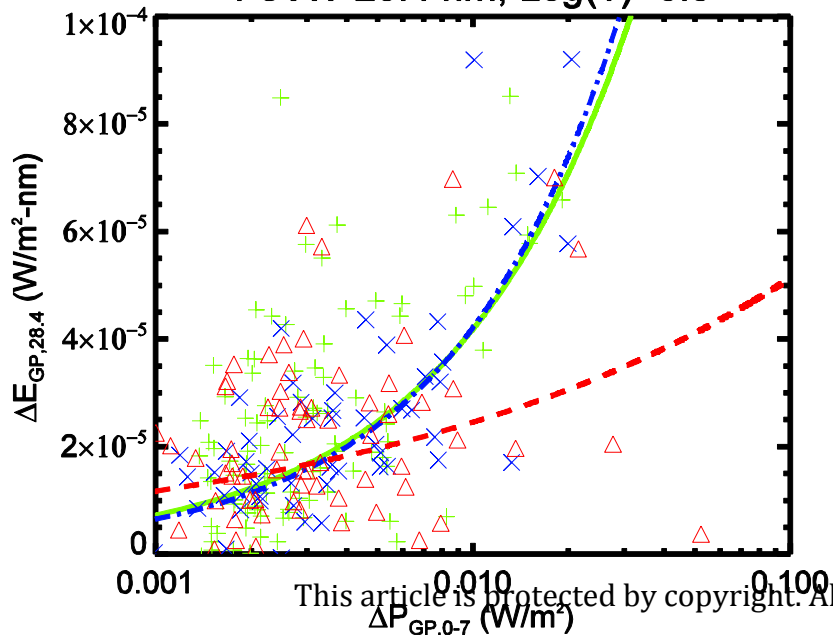
Fe XVIII 9.4 nm, Log(T)=6.96



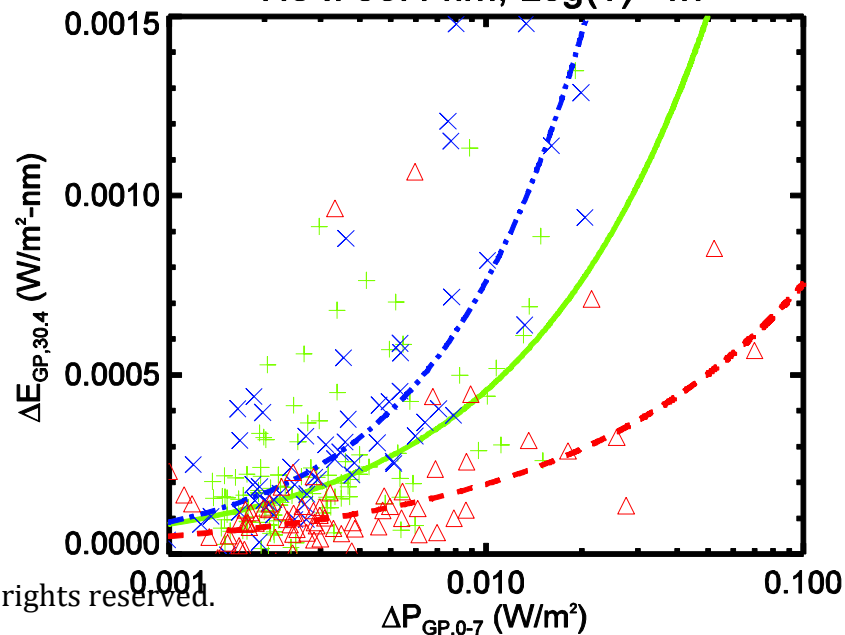
Fe XXIV 19.2 nm, Log(T)=7.2



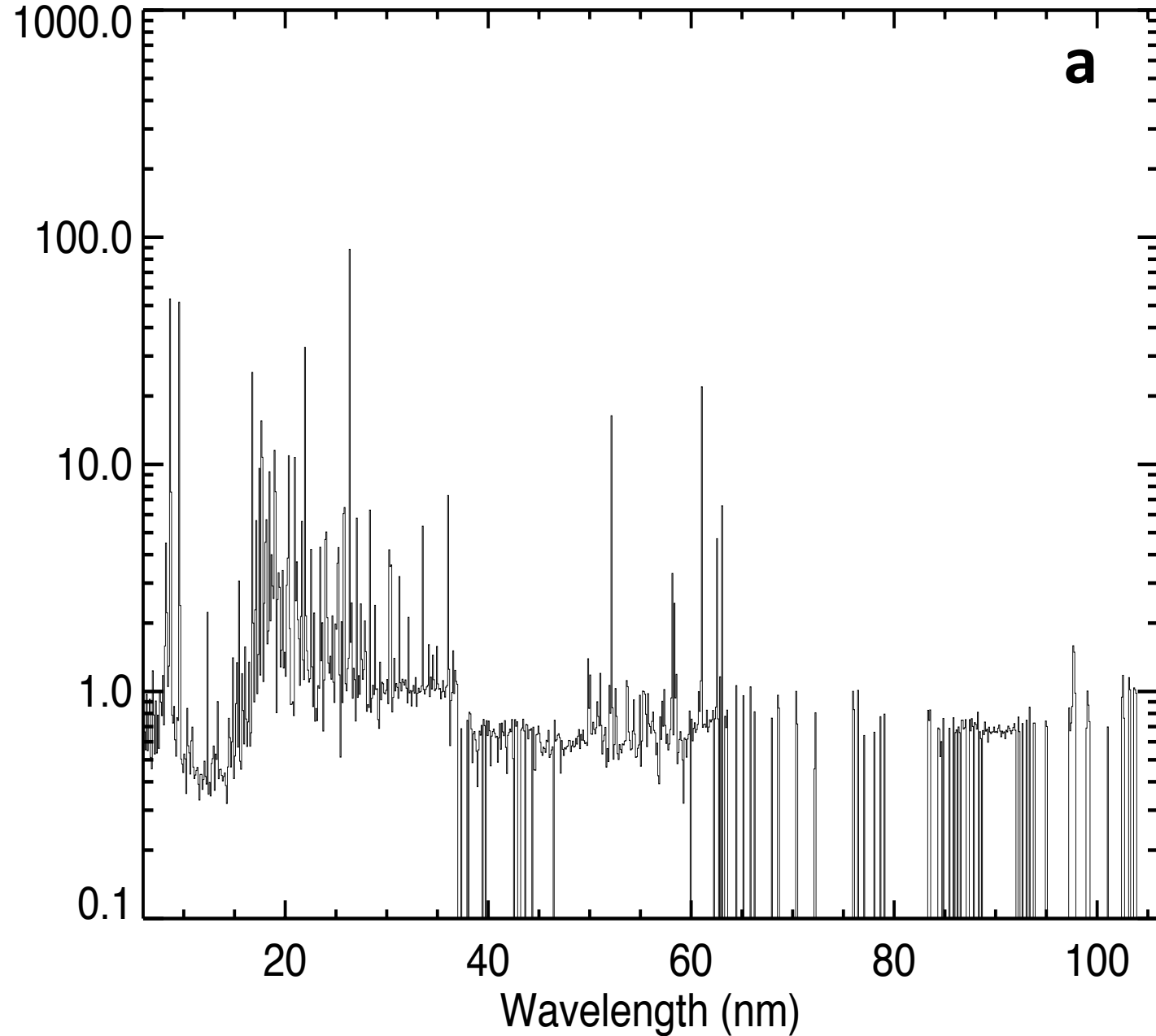
Fe XV 28.4 nm, Log(T)=6.3



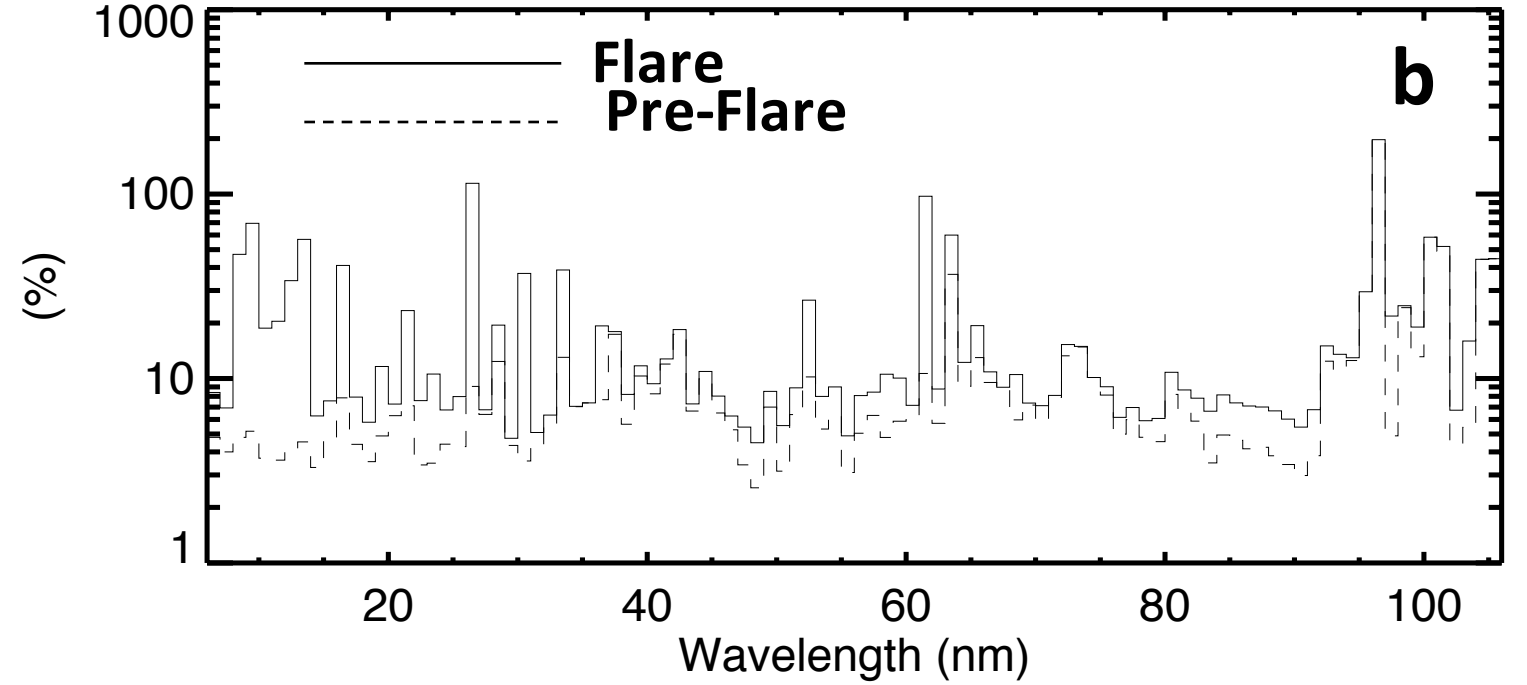
He II 30.4 nm, Log(T)=4.7



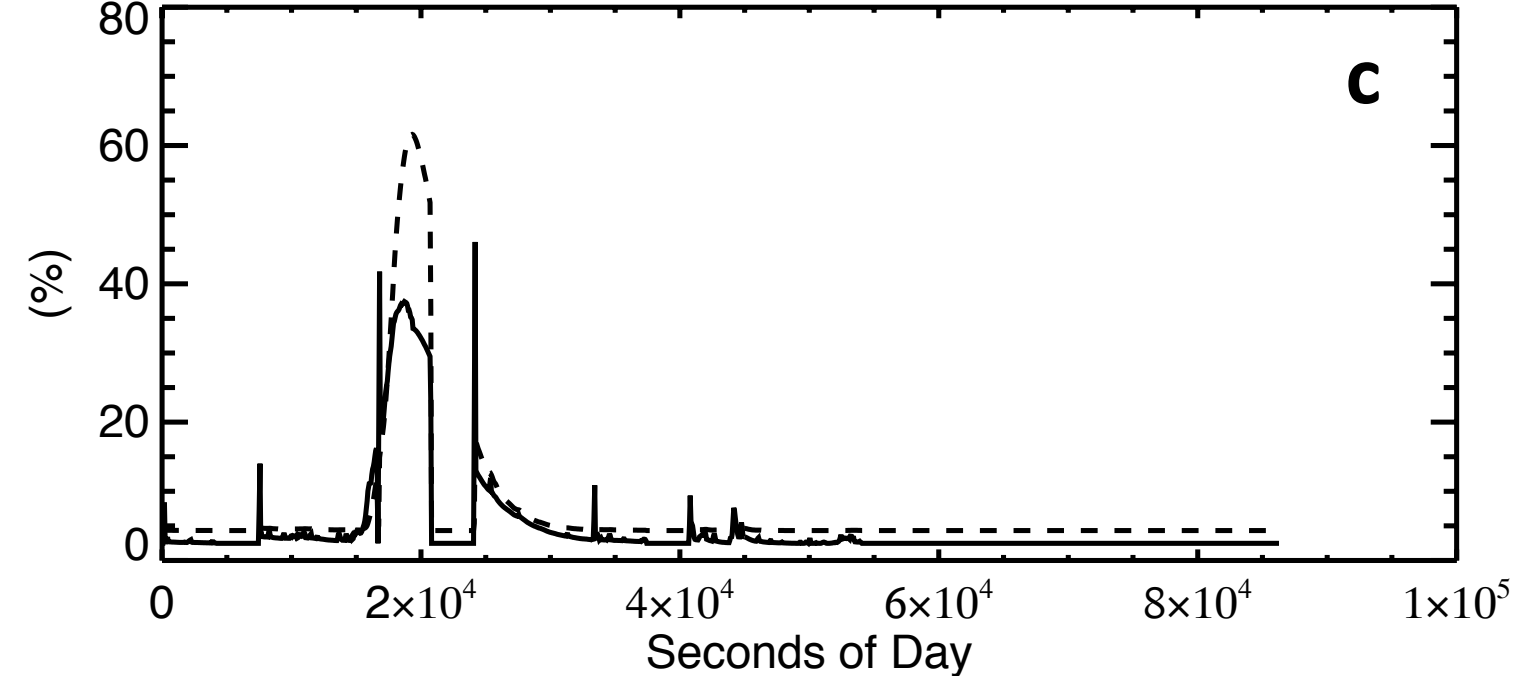
FISM-M Flare Contribution Uncertainty

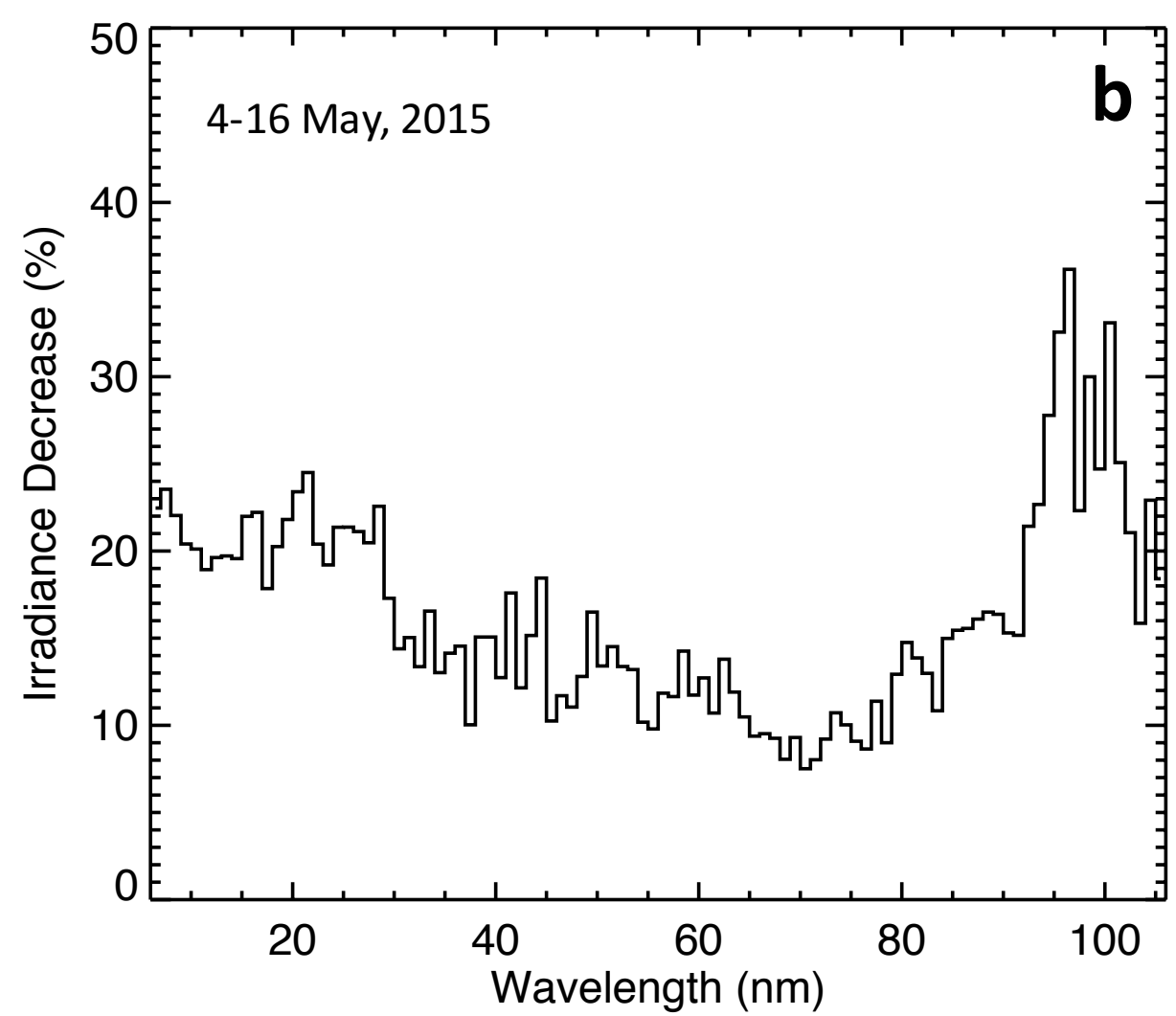
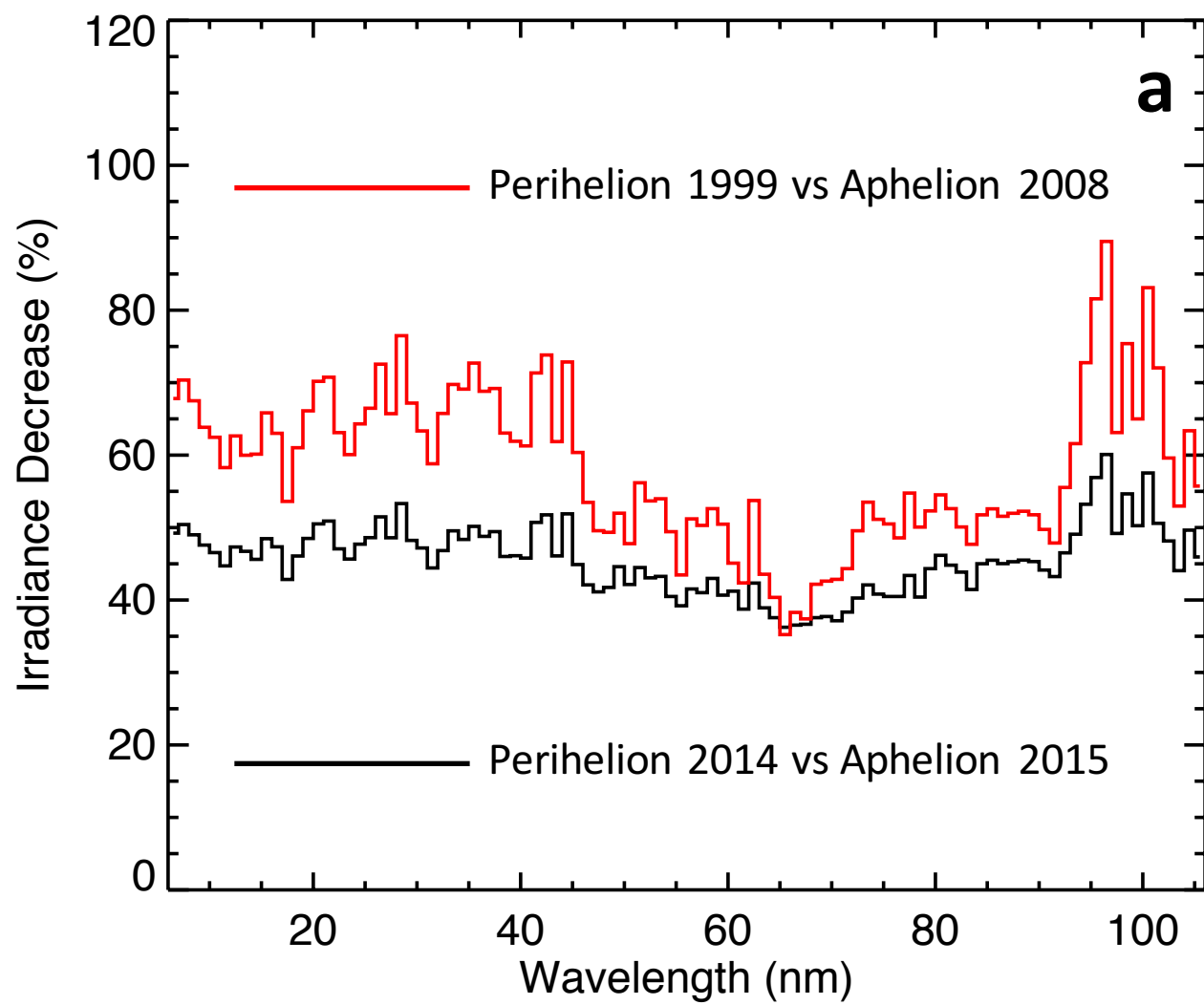


FISM-M 19-OCT-2014 X2 Flare Peak Uncertainty

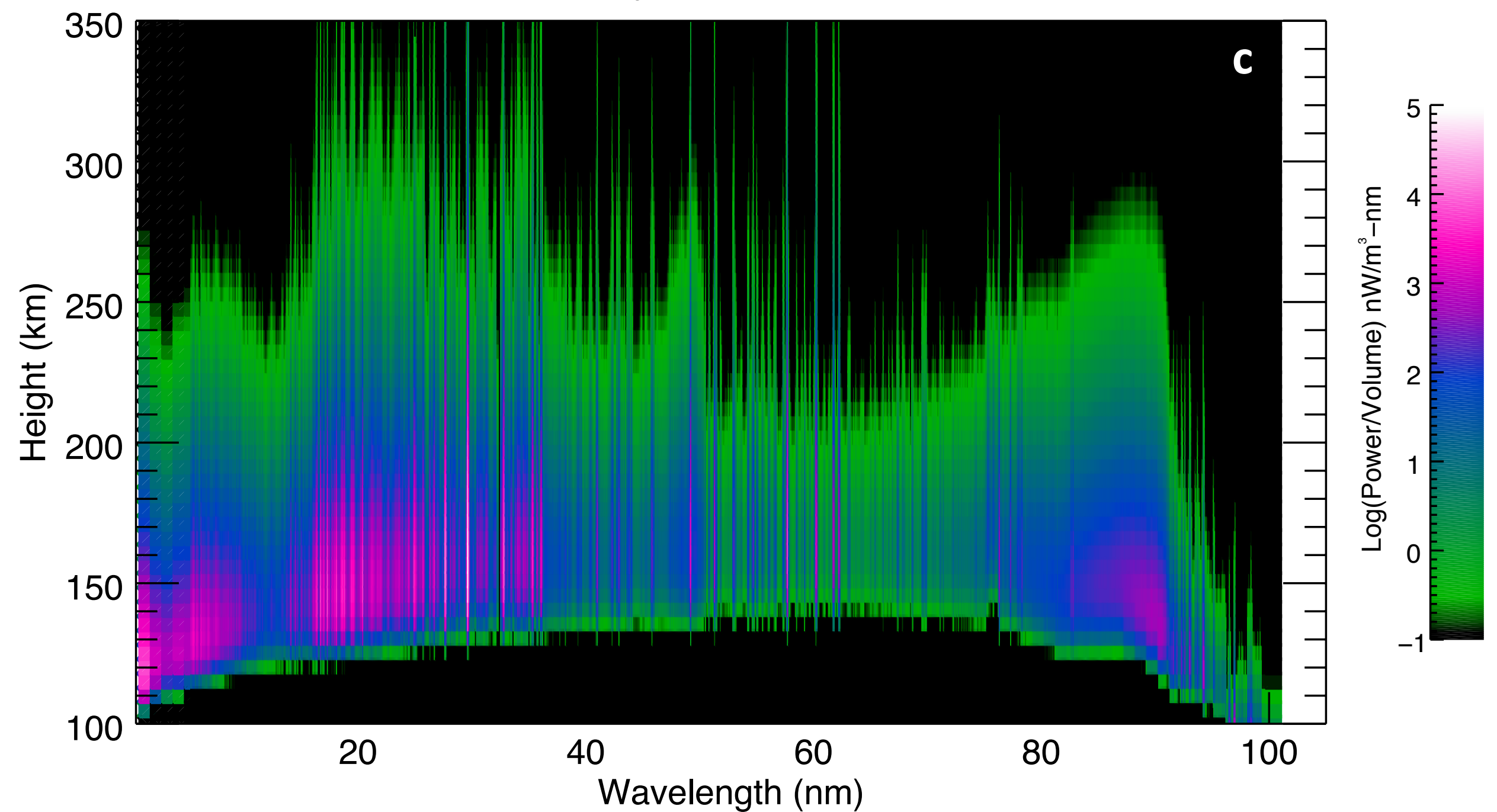


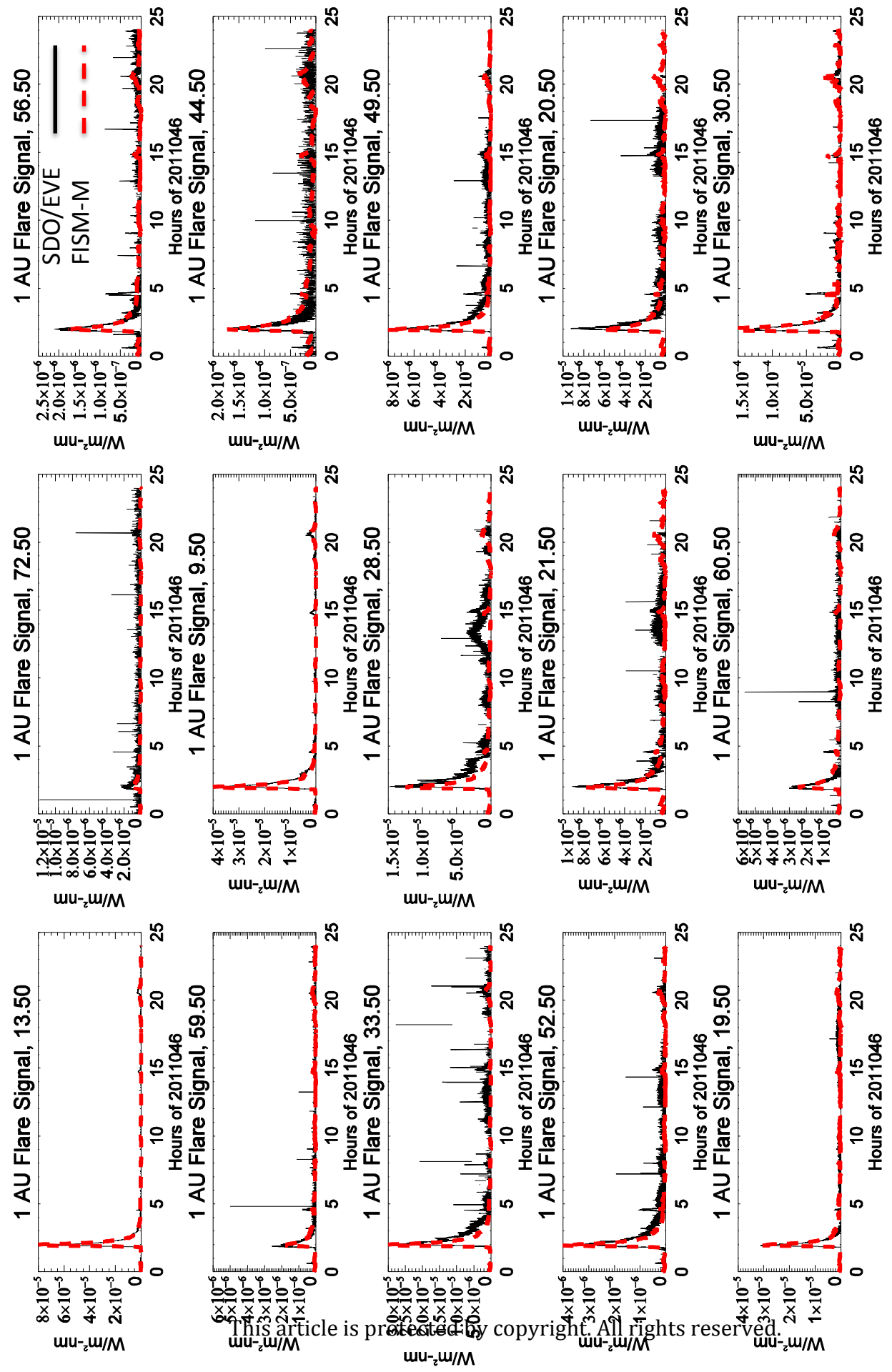
30.5 and 13.5 (---) nm Uncertainty



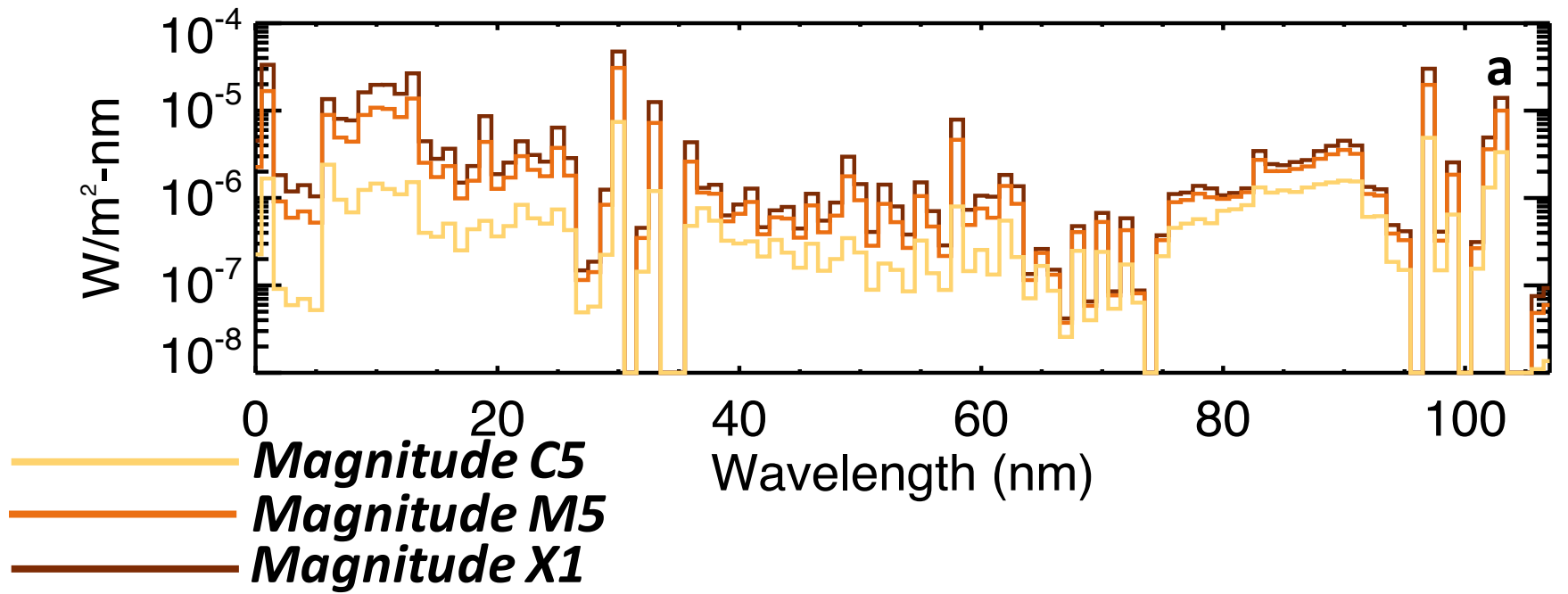


EUV Power Density Enhancement, Solar Rotation

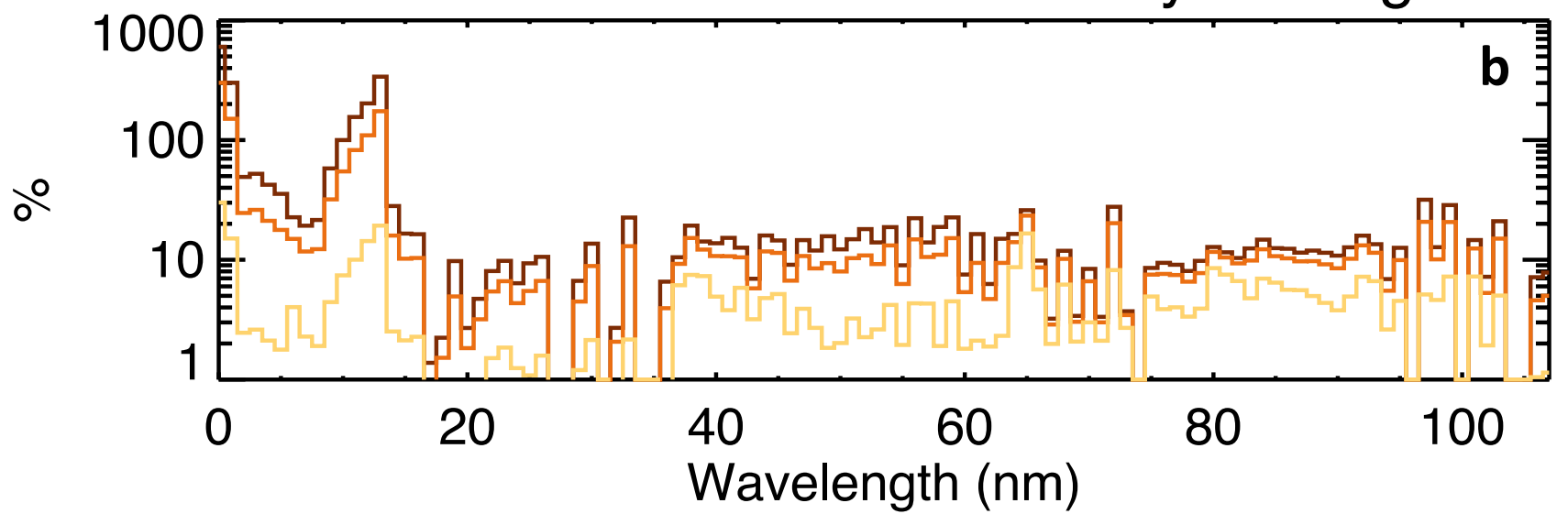




Peak Enhancement



Peak Above 1-JAN-2015 Daily Average



EUV Power Density Enhancement, X1 Solar Flare

